

THESIS

SPIN WAVE CHARACTERIZATION IN A 1D YIG MAGNONIC CRYSTAL

Submitted by
Lia Compton
Department of Physics

In partial fulfillment of the requirements
For the Degree of Master of Science
Colorado State University
Fort Collins, Colorado
Fall 2023

Master's Committee:

Advisor: Kristen Buchanan

John Harton
Amy Prieto

Copyright by Lia Compton 2023

All Rights Reserved

ABSTRACT

SPIN WAVE CHARACTERIZATION IN A 1D YIG MAGNONIC CRYSTAL

In this thesis, I will analyze and discuss features of spin wave propagation characteristics measured in a one-dimensional (1D) yttrium iron garnet (YIG) magnonic crystal using time-resolved Brillouin light scattering (TR-BLS) measurements. Magnonic crystals are a promising candidate to aid in developing spin-based devices that exploit the spin of the electron since magnonic crystals can be used to control the information transmitted by spin waves. In magnonic crystals, periodic modulation of the material properties is used to create a band structure and hence allow or suppress the propagation of spin waves with specific frequencies. To better understand spin wave propagation in a 1D YIG magnonic crystal, (TR-BLS) measurements were used to map out the temporal and spatial evolution of spin wave pulses at different frequencies. By analyzing the TR-BLS data with a cross-correlation method, the group velocities were determined at different frequencies and a better understanding of the changes in the pulse shape is gained. The TR-BLS data show that multiple width-quantized spin wave modes are present and highlights the importance of considering the two-dimensional nature of spin wave propagation, even in a one-dimensional system.

ACKNOWLEDGEMENTS

I have been incredibly lucky to have so many people supporting me as I worked towards completing this thesis that deserves recognition. I first would like to thank Kristen Buchanan for taking me on as a student. Her mentorship and guidance have helped me develop into a more confident researcher and opened my eyes further to the vast field of magnetics research.

I would also like to thank Caesar, Jason, Katie, and Mitchell for the engaging conversations. I am especially grateful for Katie and Mitchell. They both played a critical role in welcoming me to the group and helping me find my way through the lab.

Lastly, I would like to thank all my friends and family for providing constant moral support. I would not be where I am today without them.

TABLE OF CONTENTS

ABSTRACT		ii
ACKNOWLEDGEMENTS		iii
Chapter 1	Overview	1
1.1	Motivation	1
1.2	Outline of Thesis	2
Chapter 2	Background Information	4
2.1	Spin Waves	4
2.2	Magnonic Crystals	8
Chapter 3	Experimental Techniques	12
3.1	Introduction	12
3.2	Microwave Measurements	12
3.3	Brillouin Light Scattering (BLS)	14
3.4	Data	21
Chapter 4	Analysis	28
4.1	Introduction	28
4.2	Pulse Selection	28
4.3	Cross-Correlation	32
4.4	Pulse Propagation	38
4.4.1	Pulse Along the Width	38
4.4.2	Diamond Pattern	40
4.5	Group Velocity	45
4.5.1	Group Velocity using Cross-Correlation	45
4.5.2	Group Velocity using Dispersion Relation	48
4.5.3	Group Velocity for All Frequencies	50
4.6	Pulse Shape	52
4.6.1	Pulse Spreading	53
4.6.2	Pulse Shape Changes	54
4.7	Potential Future Analysis	63
Chapter 5	Conclusion	64
Bibliography		66

Chapter 1

Overview

1.1 Motivation

Research focused on working towards better and more efficient spin-based electronics has grown in importance. Traditional electronic devices use the movement of electrons to process information and are reaching their fundamental threshold. Therefore, new ideas are needed to exploit additional degrees of freedom. Research in magnetism focuses on the spin of electrons, and their interactions, as a method to process, transmit, and store information. Spin polarized electrons can carry information from one location to another and in magnetic materials, spin waves can propagate and carry information [1]. Using spin waves opens new possibilities for information transmitting without needing to move electrons.

Magnonic crystals, a magnetic material with periodic modulation of the material properties, are a promising candidate for spin-based electronics due to their tunability and size. The periodicity of material properties in a magnonic crystal affects spin waves with wavelengths on the order of the periodicity. This leads to a band structure that dictates the specific frequencies at which a spin wave can or cannot propagate. Therefore, through the magnonic crystal's material and geometry, spin wave propagation can be controlled. Similar approaches are used with light (photonics) and phonons (phononics). Spin waves can also be controlled through the system's applied magnetic field and driving frequency. Magnonic crystal's unique properties allow them to potentially be used as microwave filters, in telecommunication systems, and radar [2].

However, before magnonic crystals can be used on a larger scale, it is crucial to further understand how spin waves propagate in magnonic crystals. Previous work uses microwave measurements to gain the width-averaged information at specific location and the transmission profile of spin waves in magnonic crystals [3]. While the transmission profile is helpful to identify the band structure, it does not provide the full picture of how spin waves propagate. Imaging the

time-resolved response of a magnonic crystal is needed for a more detailed understanding. Time-resolved Brillouin light scattering (TR-BLS) is a good solution because it can be used to characterize information about spin waves like their time, phase, and wave number [4–7]. TR-BLS measurements give a better picture of where the spin wave is and how it is travelling in a magnonic crystal.

This thesis focuses on further understanding the effects of the periodic modulations in a magnonic crystal on spin wave propagation. The TR-BLS data was used to map out the propagation of a spin wave pulse in a one-dimensional (1D) magnonic crystal in space and time. The sample is categorized as a 1D magnonic crystal because the periodic modulations are in one direction. The sample is a yttrium iron garnet (YIG) film on a gallium gadolinium garnet (GGG) substrate. A YIG sample was chosen due to its low damping properties [7, 8]. The periodic modulations consist of 20 grooves chemically etched into the film using hot orthophosphoric acid. From the TR-BLS data, information like the average group velocity of the pulse and the characteristics of the pulse shape were determined.

1.2 Outline of Thesis

The focus of this thesis is on using TR-BLS data to further understand the group velocity and pulse shape of a spin wave in magnonic crystals. It is broken up into the following chapters:

Chapter 2 focuses on background information of magnonic crystals and spin waves. The characteristics of magnonic crystals and the details of the sample used are discussed. It also covers relevant information about spin waves and their properties in magnonic crystals.

Chapter 3 describes the experimental techniques used to obtain data and presents an explanation of the data analysis procedure. Microwave measurements are used to get the transmission profile and to determine the frequencies at which spin waves can or cannot propagate. Brillouin light scattering (BLS) is the main method used to observe and characterize spin wave propagation in magnonic crystals.

Chapter 4 contains a detailed analysis of the TR-BLS data. First, an overview of the analysis methods, like cross-correlation, is described. Then the results of the analysis of the average group velocities and characteristics of the pulses shape at key frequencies are presented.

The final chapter is a summary of the results and a discussion of future work.

Chapter 2

Background Information

2.1 Spin Waves

Magnetic properties of a material are due to the orbital and spin angular momentum of electrons. The magnetic moment will precess around the applied magnetic field in a cone shape, as illustrated in Fig. 2.1. The shape is similar to the precession of a spinning top. If there is a chain of electrons with spin, each spin will interact with their nearest neighbor based on dipolar and exchange interactions. Exciting one of the spins in the chain will create a cascading effect where each subsequent spin precesses but offset by a phase shift. This chain of precessing electrons is a spin wave. Spin waves are often treated as quasiparticles known as magnons.

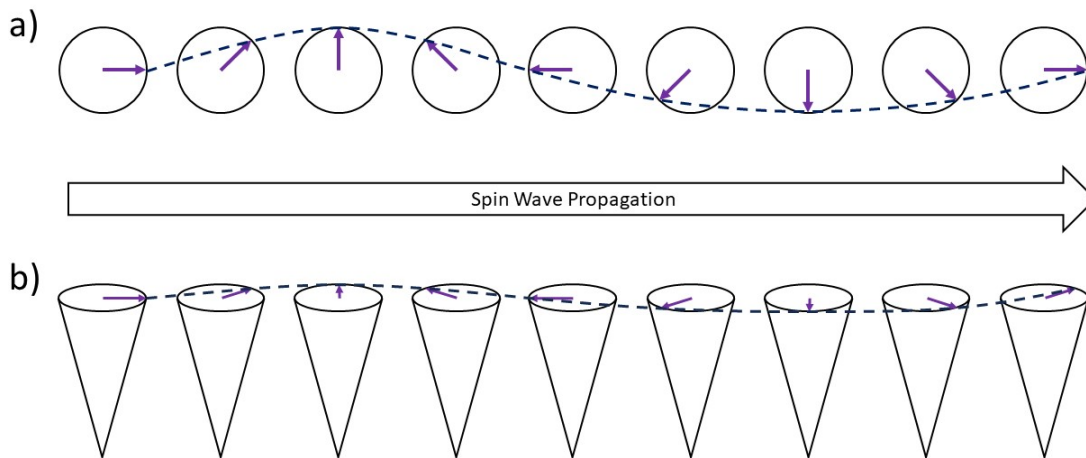


Figure 2.1: Diagram of a spin wave. (a) A top view of the spins. (b) A side view of the spins.

Spin waves are useful to transfer, store, and process information. Since they are waves, they behave similarly to that of light and sound waves. They can reflect and interfere with each other [9].

Two spin waves with the same phase will interfere constructively when they interact. Therefore, the wave and information are preserved (Fig 2.2 a). When two spin waves offset by a phase of π interact, destructive interference occurs (Fig. 2.2 b). The wave and the information are suppressed [10]. By exploiting wave interference behavior, it is possible to control the conditions for when information is preserved and when it is suppressed.

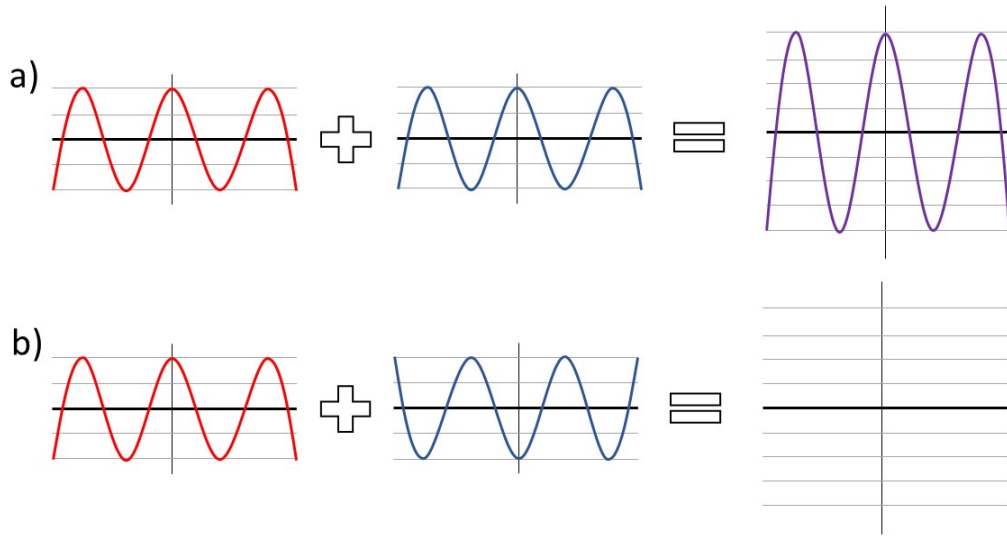


Figure 2.2: Diagram of wave interference showing (a) constructive and (b) destructive interference.

Three types of spin wave configuration can be identified based on the direction of the magnetic field with respect to the direction of spin wave propagation: forward volume spin waves (FVSWs), backward volume spin waves (BVSWs), and magnetostatic surface waves (MSSWs) (Fig 2.3). (The MSSW configuration is also commonly referred to as Damon-Eshbach modes, based on the people who discovered them [11]) The spin waves will predominantly radiate perpendicular to the antenna. The configuration of the system will greatly affect the dispersion relation and the spin wave behavior [12]. For example, features such as the group velocity and lifetime will vary. The experiment done in this thesis focuses on the MSSW (surface wave) configuration.

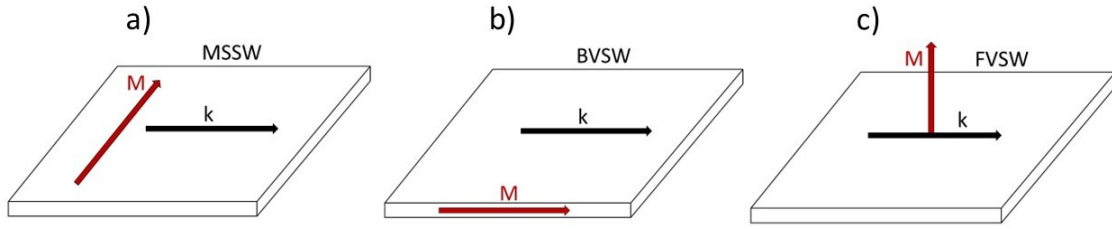


Figure 2.3: Diagram of the three different configurations for spin waves. The direction of the magnetization is indicated by the red arrow and the direction of propagation of the spin waves is indicated by the black arrow, where k is the wave vector. a) is the magnetostatic surface wave configuration (MSSW), the configuration used for this work. b) is the backward volume spin wave configuration (BVSW). c) is the forward volume configuration (FVSW).

While MSSWs in magnonic crystals have been studied less, there are many advantages to using the surface wave configuration compared to the backward or forward volume configuration to excite spin waves. In the surface wave configuration (Fig 2.3 a), spin waves propagate in-plane and with the magnetic field perpendicular to the direction of propagation. The components of the dynamic field from the stripline antenna are perpendicular to the static magnetization and leads to spin waves from the torque on the magnetic moment. The excitation efficiency from the antenna is greater for MSSWs as compared to BVSWs because two components of the dynamic field contribute to the excitation, whereas for BVSWs only one component contributes to the excitation. Also, the group velocity for MSSWs is generally faster than BVSWs and MSSWs also exhibit a non-reciprocal propagation in the magnetostatic (low wavevector) regime, which can be useful for applications. The slope for the dispersion relation for MSSWs is positive for positive frequencies (Fig 2.4). Therefore, the group velocity and the phase velocity are in the same direction. Whereas in the backward volume configuration, spin waves have a symmetrical excitation in their propagation. The forward volume configuration, in contrast, features isotropic spin wave propagation [3, 5, 6, 8, 11, 13–15].

Characteristics of a spin wave such as the energy, frequency, and wave vector are described through its dispersion relation [1, 12]. The dispersion relation relates the oscillatory frequency of the spin wave (ω) to its wave vector (k). It is used to understand how any type of wave will

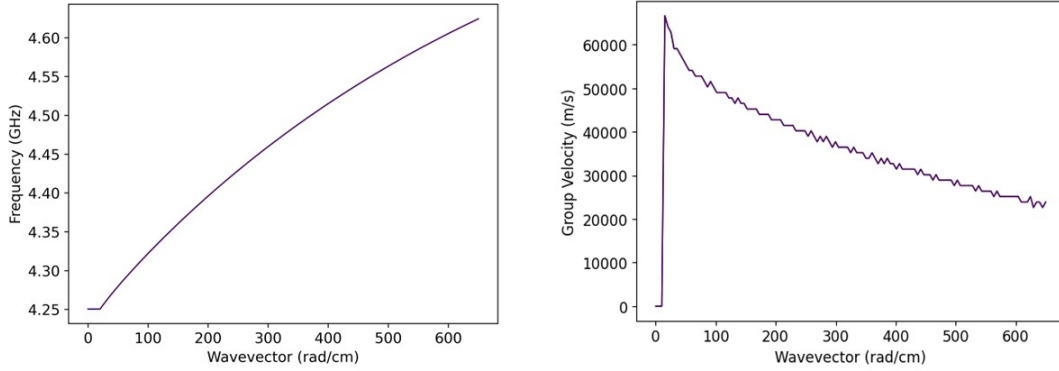


Figure 2.4: Representative dispersion relation and corresponding group velocity, calculated using the material parameters and thickness of the yttrium iron garnet (YIG) thin film used for the 1D magnonic crystal discussed in this thesis. (Applied magnetic field is 855 Oe)

behave. In a typical spin wave experiment, spin wave pulses are excited at GHz frequencies using an antenna. The dispersion relation gives the wavevector and phase velocity ($v_p = \frac{\omega}{k}$) for a specific frequency. The phase velocity is the rate at which the wave with a specific phase propagates through a medium [16]. The group velocity ($v_g = \frac{d\omega}{dk}$) is the velocity of a wave packet as it propagates through the medium. This is also the velocity at which energy propagates, and v_g can be obtained from the slope of the dispersion relation.

Depending on the orientation of the sample and the direction of the magnetic field, the dispersion relation can vary. The thickness and material of the sample can also affect the dispersion relation [2]. For the surface wave configuration, the dispersion relation generally shows that with increasing k there is an increase in frequency due to dipolar interactions. Then the dispersion relation levels off at intermediate k and goes as k^2 for high k due to exchange interactions (Fig. 2.5). Our experiment focuses on the magnetostatic (dipole-dominated, low wavevector) range, and the group velocity tends to reach a maximum at small wavenumbers in this regime [1].

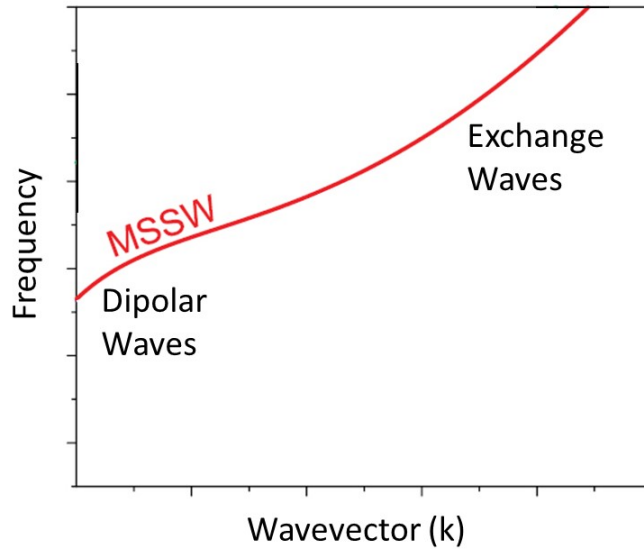


Figure 2.5: The dispersion relation for MSSWs for dipolar and exchange interactions. (Modified from Ref [1])

2.2 Magnonic Crystals

The theory behind the dynamics in photonic crystals gave rise to magnonic crystals. Photonic crystals are used to direct light into certain zones or to disrupt the propagation of light [17]. They have been used for technology like logic functions, polarizers, and filters by controlling information through constructive and destructive interference of light. When there is destructive interference, a band gap is created, and the transmission of information is suppressed. Photonic crystals control the propagation of electromagnetic waves, while magnonic crystals provide a similar function to control spin waves [18].

Both photonic and magnonic crystals use periodic modulation of the material properties to control the propagation of spin waves. The periodic modulations in magnonic crystals create band gaps that disrupt the propagation of spin waves at specific frequencies [19]. The disruption of the spin waves is due to the Bragg reflection of the spin waves off of physical barriers and the reflected waves destructively interfere with the incoming spin waves. Therefore, based on the design of the magnonic crystal, particular wavevectors can pass, and some cannot. The frequency ranges of the

band pass and band gaps can be tuned by selectively choosing the magnonic crystal's geometry, magnetic field, and materials.

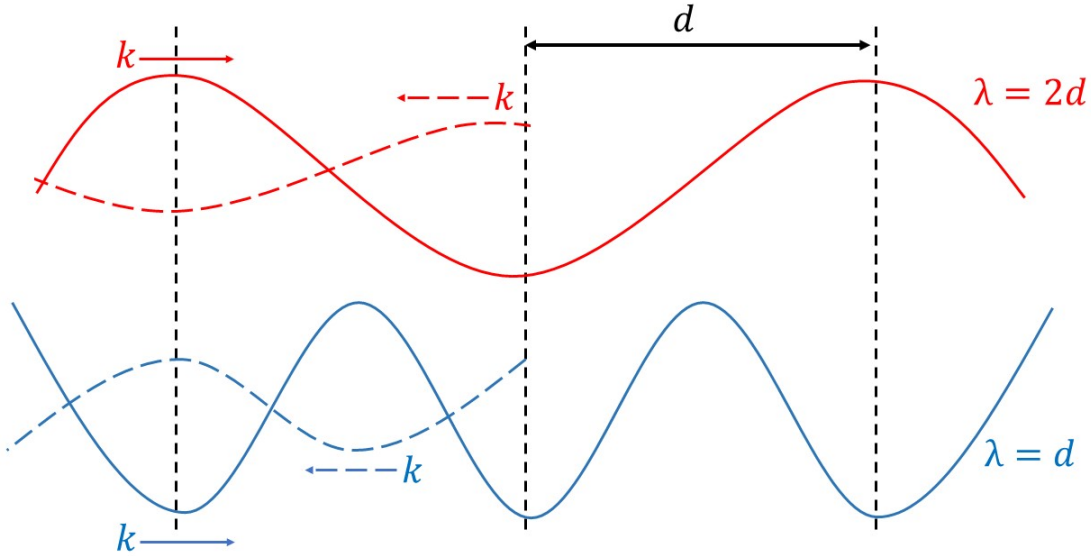


Figure 2.6: Diagram of spin waves reflecting off of the grooves in the crystal. The colored solid lines show the magnetic oscillations of the transmitted waves at an instant in time, and the colored dashed lines show the reflected waves. The grooves of the 1D magnonic crystal that serve as reflectors are represented with the black dashed lines, separated by distance d . The transmission and reflection amplitude are not to scale.

The interest in magnonic crystals grew due to their size and potential for more efficient spin-based devices. Spin waves have a short wavelength, on the nanometer scale. For example, a 4 GHz wave in vacuum has a wavelength of 75 mm, whereas a spin wave in a YIG film at the same frequency has a wavelength of around $10 \mu\text{m}$ and can extend into the nanometer scale [2]. Devices based on spin waves also do not rely on the movement of electrons and reduce the risk of heating up and provide a means to transmit information through electrically insulating materials.

The magnonic crystal used in this experiment is a one-dimensional (1D) YIG magnonic crystal. It is defined as a 1D magnonic crystal because the pattern is repeating in only one direction. YIG is a common choice for magnonic crystals because of its low damping and strong tunability for the group velocity [14]. Low damping means the lifetime of a spin wave is longer compared to

other materials [2, 3, 8]. For example, a surface spin wave with a wavelength of $\lambda = 1 \mu\text{m}$ in a YIG micrometer-thick film can last upwards of microseconds. Compared to other materials, spin waves can only last tens of nanoseconds. Spin waves can also travel farther, e.g. centimeters, which is longer comparatively to metals whereas the distances are tens or hundreds of microns [1].

The sample is $6.4 \mu\text{m}$ thick and 2.25 mm wide yttrium iron garnet (YIG) film on a gallium gadolinium garnet (GGG) substrate. The film was patterned with 20 grooves with width of $a = 25 \mu\text{m}$ and depths of $3.5 \mu\text{m}$ by chemical etching using hot orthophosphoric acid. The grooves were separated by a flat region with an overall center to center spacing of $275 \mu\text{m}$. The first groove is $750 \mu\text{m}$ from the first measurement, which is 1 mm from the antenna. (Fig. 2.7). The groove profile was measured by Mitchell Swyt, another group member, using profilometry (Fig. 2.8).

The work presented in this thesis is collaborative. The sample was fabricated by Cesar Romero at the Universidad Nacional Autonoma de Mexico and Jason Liu at Georgia Southern University assisted in setting up the time-resolved equipment. Initially M. Swyt, another group member, and I made network analyzer measurements to identify the pass band and the band gap frequencies. M. Swyt then ran the TR-BLS measurements at the selected frequencies, measured the groove profile using profilometry (Fig. 2.8), and mapped out the spin wave propagation through the crystal. I ran some of the initial TR-BLS measurements and conducted the analysis of the time-resolved dataset presented in this thesis.

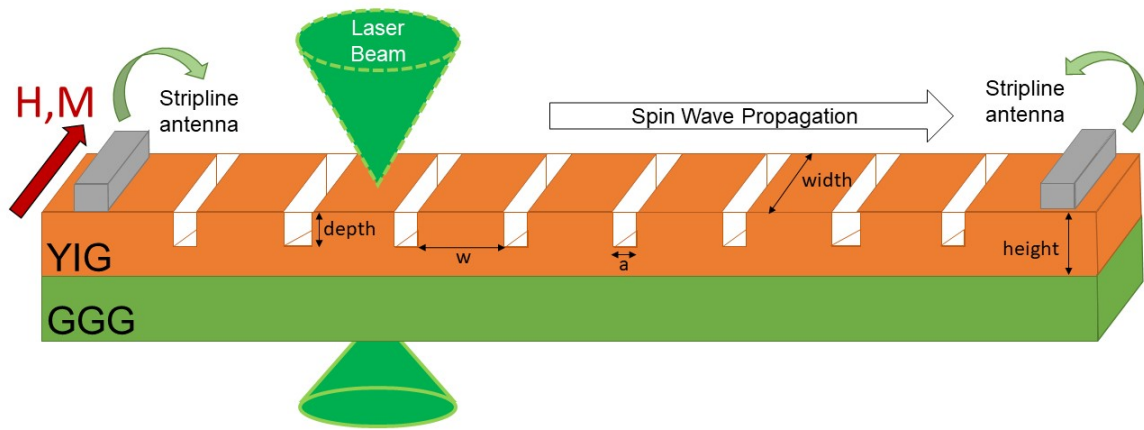


Figure 2.7: Schematic of the experimental set up. The applied magnetic field, red arrow, is 850 Oe. The sample is $6.4 \mu\text{m}$ thick, 2.25 mm wide, yttrium iron garnet (YIG) on a gallium gadolinium garnet (GGG) substrate. On each end of the crystal a stripline antenna is attached. The period pattern was chemically etched into the film using hot orthophosphoric acid. There are 20 grooves with widths of $a = 25 \mu\text{m}$ and depths of $3.5 \mu\text{m}$. Each groove is separated by a $w = 250 \mu\text{m}$ flat region.

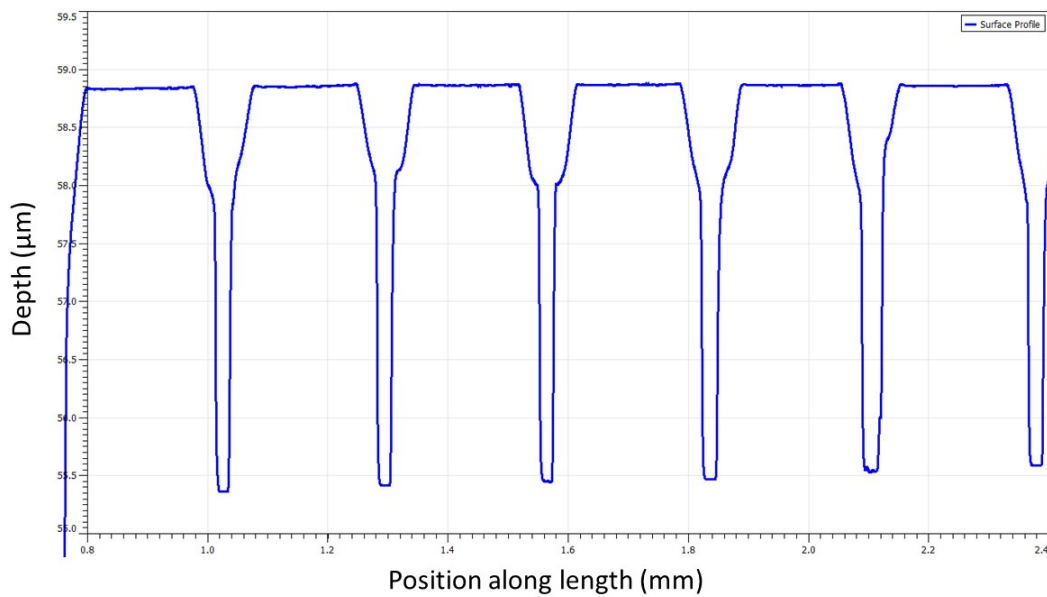


Figure 2.8: The profile of magnonic crystal grooves measured by Mitchell Swyt via profilometry.

Chapter 3

Experimental Techniques

3.1 Introduction

In this section, a description of the experimental techniques used and an explanation of the TR-BLS data will be discussed. The microwave measurements using the vector network analyzer (VNA) provided the transmission profile. From the transmission profile, four driving frequencies, the band pass and band gaps, were selected for TR-BLS measurements. The next section is a detailed explanation and schematic of the TR-BLS system. The last section steps through the analysis procedure to interpret the TR-BLS data.

3.2 Microwave Measurements

A vector network analyzer (VNA) was used to measure the transmission loss as a function of frequency of the 1D magnonic crystal. The S-parameter from the VNA shows the transmission loss, in dB, measured at specific frequencies [20]. A microwave signal is sent from the VNA to the antenna attached to the magnonic crystal to excite spin waves, as shown in Fig. 3.1. The S-parameter, S_{12} , compares the signal from the output antenna with the signal launched at the input antenna. Stripline antennas with widths of approximately $50 \mu\text{m}$ were used to launch and receive the spin waves. The transmission loss was measured for frequencies between 4.0 – 5.0 GHz with an applied magnetic field of $H = 855 \text{ Oe}$.

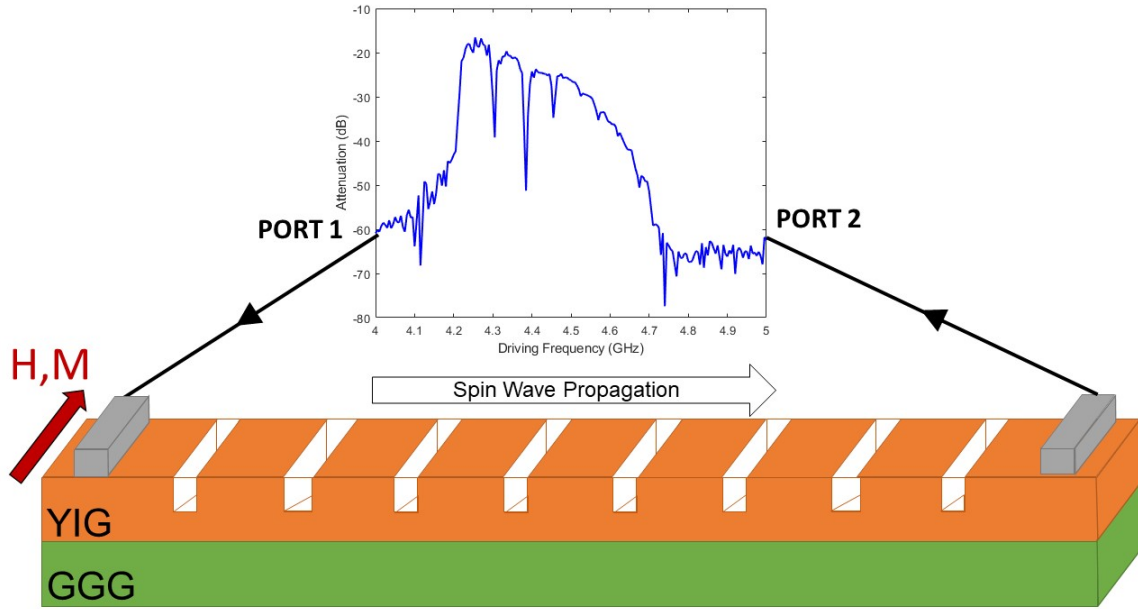


Figure 3.1: Diagram of the sample connected to vector network analyzer (VNA) to obtain transmission profile. The spin waves are launched from the left antenna (gray bar attached to port 1), and received by the right antenna (gray bar connected to port 2).

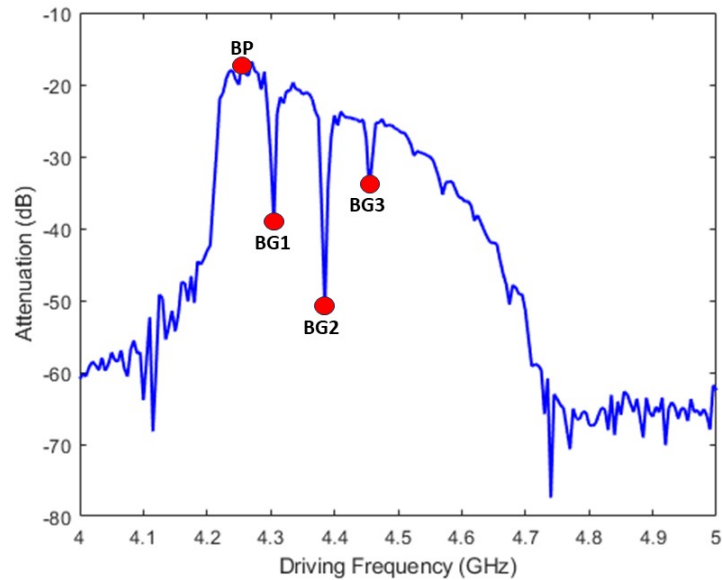


Figure 3.2: The 1D magnonic crystal transmission profile (solid line) with the four frequencies selected for TR-BLS measurements, shown as red circles and labeled as band pass (BP) and band gaps (BG1-BG3).

Fig. 3.2 shows the measured transmission profile of the 1D magnonic crystal. The attenuation from the input to the output antenna is indicative of how well the spin wave signal can propagate from one end of the magnonic crystal to the other. If spin waves propagate efficiently through the magnonic crystal, then the attenuation value will be larger. For example, driving the system at 4.25 GHz results in the largest value of attenuation. Therefore, spin waves can propagate easily at this frequency. This frequency is known as the band pass (BP). When there is a sharp drop in attenuation, that frequency is called the band gap (BG). At BG frequencies the spin waves cannot propagate as easily because the periodic pattern in the magnonic crystal leads to destructive interference of the spin waves.

Microwave measurements have been used before with other magnonic crystal experiments [3]. While these measurements are helpful to identify the band structure, they do not give any spatial or temporal information about spin wave propagation in magnonic crystals. To obtain additional details, imaging techniques can be used, like time-resolved Brillouin light scattering.

Based on the transmission profile (Fig. 3.2), the following frequencies were chosen to observe spin waves in more detail using TR-BLS.

Table 3.1: Table of the band gap and band pass frequencies identified in Fig. 3.2.

Name	Frequency (GHz)
Band Pass (BP)	4.25
Band Gap 1 (BG1)	4.305
Band Gap 2 (BG2)	4.38
Band Gap 3 (BG3)	4.455

3.3 Brillouin Light Scattering (BLS)

Time-resolved Brillouin light scattering (TR-BLS) measurements can be used to obtain both spatial and temporal information on spin waves. Brillouin light scattering (BLS) is a measurement

technique used to study magnons by utilizing the information from inelastically scattered photons from a laser probe with magnons in the sample. When the photons are inelastically scattered, energy is conserved, and the scattered photons are frequency-shifted. This frequency shift is due to the energy released or absorbed by the magnon; known as the Stokes and anti-Stokes processes, respectively. The Stokes process leads to a negative frequency shift and occurs when a photon gives up energy to create a magnon. The anti-Stokes process leads to a positive frequency shift and a magnon is annihilated in the scattering process. The frequency shift of the inelastically scattered photon is equal to the frequency of the magnon. For thin films, the in-plane momentum is also conserved in the scattering process, so the angle dependence of the scattering process can be used to obtain information on the magnon wavenumber. The intensity of the scattered photons is also proportional to the intensity of the magnons [3, 21].

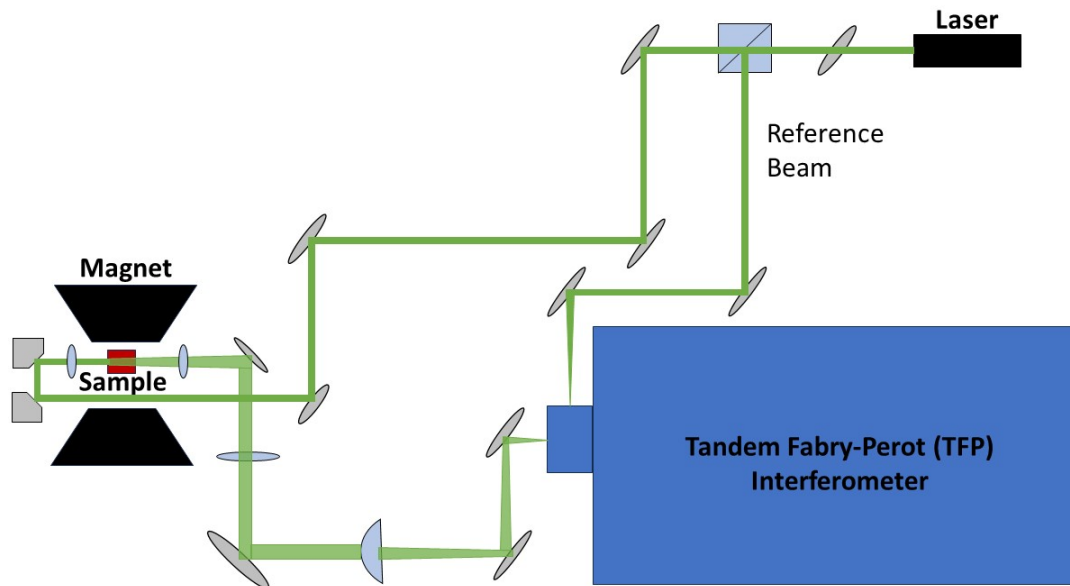


Figure 3.3: A schematic of the optics and instruments used for the forward scattering BLS measurements. The green lines represent the laser path, the grey shapes represent the mirrors, and the light blue shapes represent the lenses. The TFP is used to detect the frequency shifted photons.

Fig. 3.3 shows a schematic of the optical beam path guiding the laser to the sample and the inelastically scattered photons to the interferometer. A 532 nm single mode, linearly polarized,

laser is sent through a series of mirrors and polarizers to the sample. The mirrors guide the laser to the sample and the inelastically scattered photons are rotated by 90 degrees with respect to the input polarization. A polarizer is used to exclude elastically scattered light and ensures the polarization of the inelastically scattered light matches the polarization needed by the interferometer. A forward scattering configuration, where the light is transmitted through the sample, is used because the magnonic crystal is transparent. Another advantage of using the forward scattering configuration is that more scattered light can be collected as compared to a backscattering configuration where part of the beam is lost. Once the laser hits the sample, a cone of the inelastically scattered light is directed into the interferometer via a focusing lens that takes all the scattered light and focuses it into the interferometer input pinhole. A separate set of mirrors guides a reference beam into the side of the interferometer. The reference beam is used to monitor the laser stability and help with alignment [22, 23].

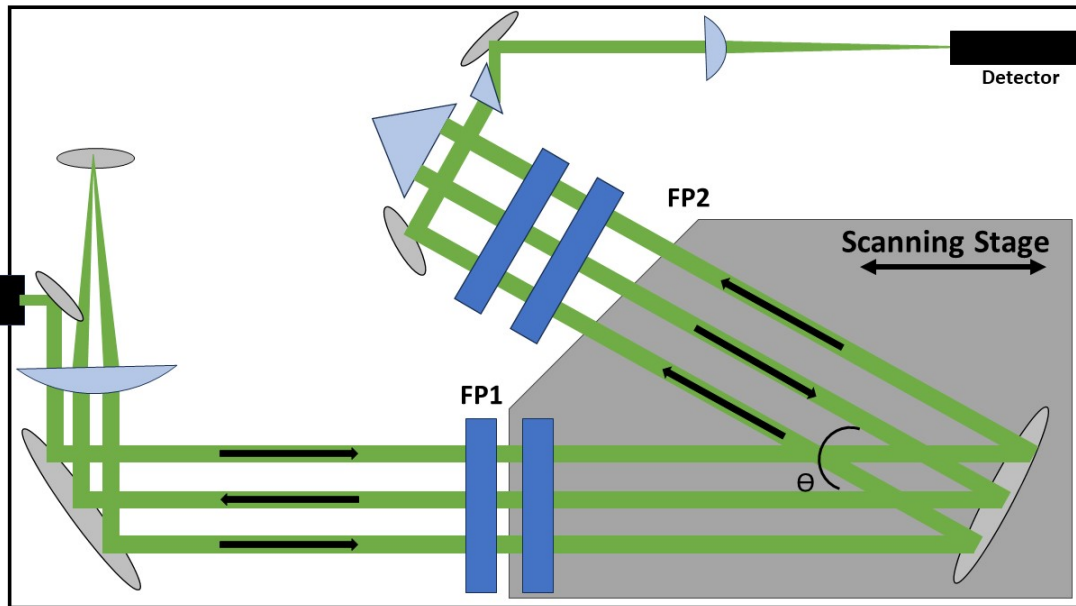


Figure 3.4: Schematic of the tandem Fabry-Perot interferometer. The single sided arrows show the direction of the beam as it passes through the etalons. The double sided arrow indicate the direction the scanning stage, the dark grey shaded area, can move to change the spacing between the mirrors, and θ is the angle between the two interferometers

A TableStable/JRS six pass tandem Fabry-Perot interferometer upgraded with the TFP-2 HC optics and a Hamamatsu C11202-50 detector was used for data collection in this thesis. A key element in the BLS system is the tandem Fabry-Perot interferometer, where two Fabry-Perot interferometers are arranged in tandem. Fig. 3.4 shows a full schematic of the interferometer. A Fabry-Perot interferometer is an optical arrangement consisting of two parallel mirrors, etalons, slightly offset with highly reflective coating [23, 24]. There are many advantages to using the tandem Fabry-Perot interferometer instead of the single Fabry-Perot interferometer. The light passes through the etalons a total of six times in the tandem version, which increases the contrast of the signal to noise ratio by filtering out weaker signals. The tandem setup also allows for unambiguous identification of the transmitted light. When using one Fabry-Perot the given frequency is transmitted strongly at regular intervals for each of the mirror sets and frequencies can be identified precisely but cannot be identified unambiguously. The slight offset of the mirror spacing for the tandem setup allows the unambiguous identification of the frequency shift. More information about the tandem Fabry-Perot set up can be found in reference [23].

ThaTEC's TFPDAS5 software is used for the data collection and piezoelectrically controlling the tandem Fabry-Perot interferometer etalon mirrors. The z control changes the distance between the mirrors by moving the scanning stage. The x and y controls are used to adjust the mirrors to make them parallel to each other. The TFPDAS5 software can manually control the mirror position and is also used to automatically stabilize the mirror position and keep them parallel during measurements.

The position of the scanning stage in Fig. 3.4 is scanned to allow different frequencies to pass through to the detector, and the number of counts is recorded as a function of the stage position. The light will pass three times through the first Fabry-Perot interferometer (FP1), with a mirror spacing L_1 . Then it passes another three times through the second Fabry-Perot interferometer (FP2), with a mirror spacing L_2 . L_1 and L_2 change simultaneously and since the spacing between the mirrors are slightly offset, FP1 and FP2 allow slightly different wavelengths of light to transmit. An example of the combined intensity profiles from FP1 and FP2 are shown in Fig. 3.5. There are

also “ghost” peaks after the two intensity profiles are combined. When the elastic signal is strong, the ghost peaks are stronger.

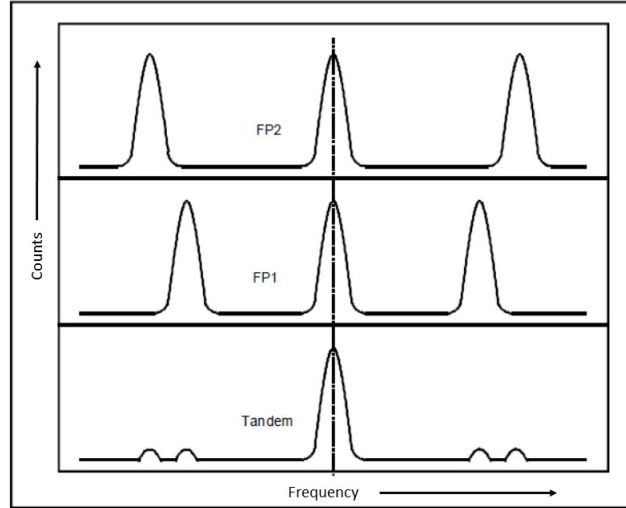


Figure 3.5: An example of the tandem Fabry-Perot interferometer transmission spectra. This figure was reproduced from Ref [24].

The value of L_1 determines the free spectral range (FSR). The FSR is the frequency range scanned by the mirrors when they move $\lambda/2$, where λ is the wavelength of the reference beam.

$$\Delta\lambda = \frac{\lambda^2}{2L_1} \quad (3.1)$$

The FSR range is centered around the frequency of the laser. During a measurement, the mirror spacing moves through the FSR and the inelastically scattered photon signal within the frequency range is recorded by the TFPDAS5 software when it arrives at the detector. A timed shutter system allows the inelastically scattered photons outside of the laser frequency to enter the interferometer, while the input beam is blocked when the mirrors scan through a region near the laser frequency. This is to protect the detector from the strong elastically scattered signal [23].

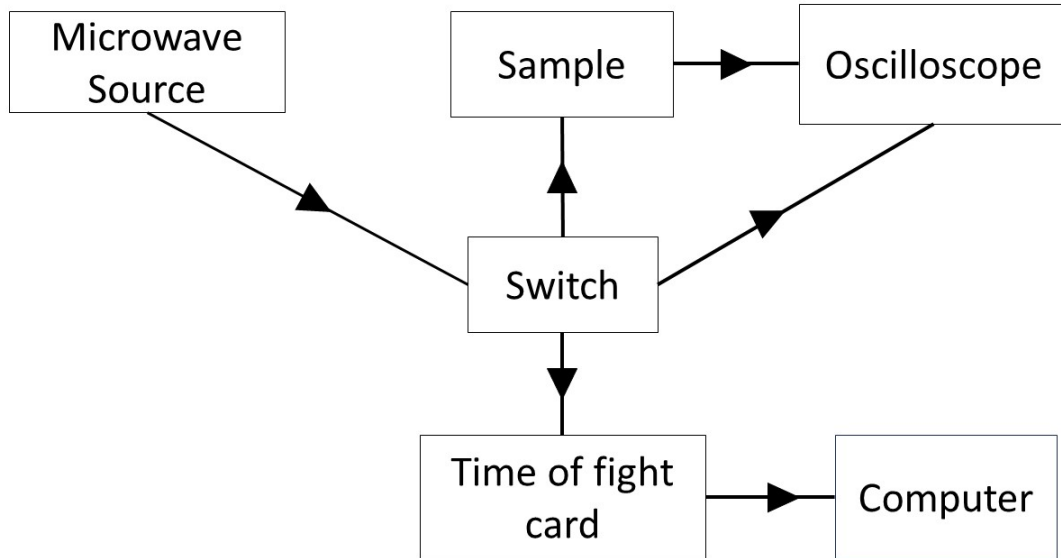


Figure 3.6: A simplified diagram of how the time-resolved setup works for the BLS system. The microwave source puts out a continuous microwave excitation at the selected frequency. The microwave pulse duration and repetition rate are set using a pulse generator connected to a microwave switch. An oscilloscope is used to check the input and output signal from the sample. The pulse generator also sends a timing trigger to a fast time of flight measurement card (250 ps temporal resolution).

ThaTEC's P7887 software is used to control the time-resolved aspect of the BLS measurement by tracking the time-of-flight of photons. A pulse generator is used to trigger the microwave switch to generate a pulsed microwave current, which is sent to the input antenna connected to the sample and generates spin waves. The sample output antenna and the microwave switch are connected to an oscilloscope to check the output and input signals. The pulse generator also sends a pulse to the time-of-flight card, which serves as a trigger for the time-of-flight counter. The pulse duration was set to 200 ns with a 1250 ns repetition rate.¹

The P7887 takes the reference counter information from the time-of-flight card and BLS detector to plot the counts versus frequency and time. Fig. 3.9, in section 3.4, shows a representative raw dataset. Now the timing of when a photon interacted with a magnon at a specific spot is

¹Our collaborators Cesar Romero at the Universidad Nacional Autonoma de Mexico and Jason Liu at Georgia Southern University assisted with setting up the microwave switch.

known. The spatial resolution for the system is $50 \mu\text{m}$, limited by the laser spot, and the temporal resolution is 250 ps , limited by the temporal resolution of the time-of-flight card. Measurements started 1 mm from the input antenna. By repeating this measurement process for multiple locations along the crystal, the spin wave propagation can be mapped spatially and temporally (Fig. 3.7). Therefore, the spin wave pulse can be tracked as it travels down the length of the crystal and the changes in the pulse shape over time can be characterized.

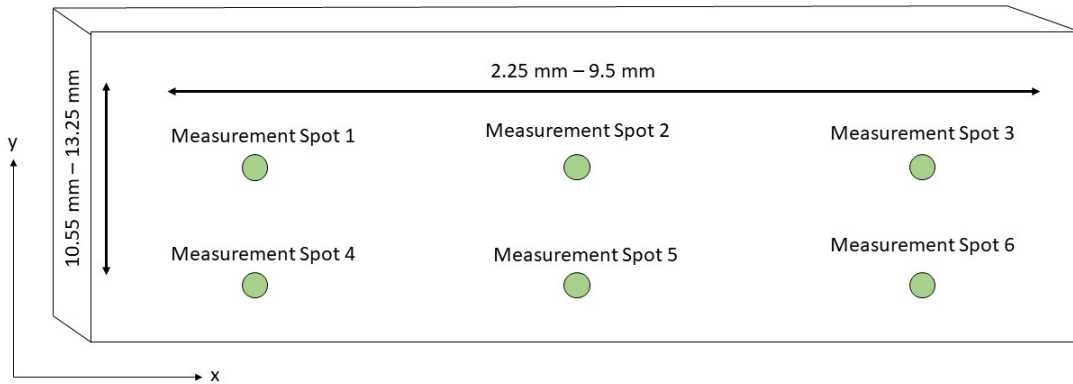


Figure 3.7: To obtain spatial maps of the spin wave propagation pattern, the laser spot is moved to different points along the sample. The length scan range (x direction) is between 2.25 mm - 9.5 mm with 146 steps of 0.05 mm . The width scan range (y direction) is 10.55 mm - 13.25 mm with 55 steps of 0.05 mm . These values are based on the micrometer positions, not the dimensions of the sample.

3.4 Data

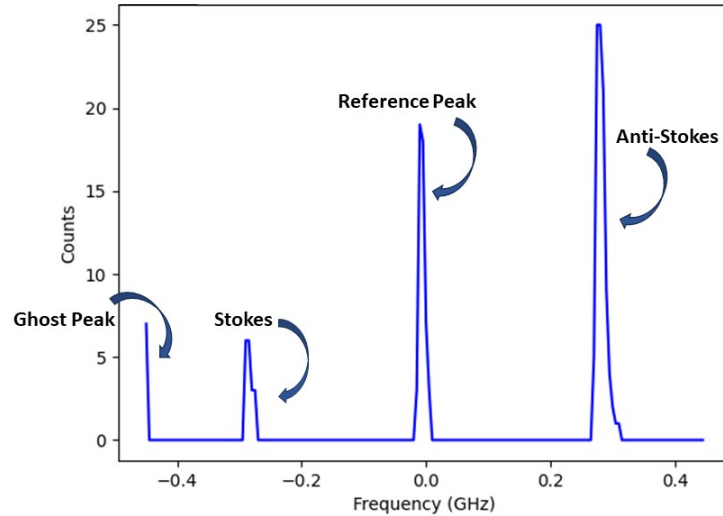


Figure 3.8: An example of raw BLS data taken at one position and one point in time. The center peak is the reference peak centered on the frequency of the laser. The left peak is the frequency shift from the Stokes process, magnon creation, and the right peak is the frequency shift from the anti-Stokes process, magnon annihilation. On the far left there is part of the ghost peak.

Fig. 3.8 shows a raw BLS spectrum obtained at one position on the sample at a specific time. The magnetic field is 855 Oe and the driving frequency is at BP (4.25 GHz). The spectrum shows the number of counts that reach the detector at different frequencies. The frequency shifts are centered around the frequency of the laser. The center peak (at $f = 0$) are counts from the reference beam, and the peaks to the left and right are the frequency shifts of the photon interacting with a magnon, the Stokes and anti-Stokes, respectively. The frequency shifts associated with these peaks coincide with the pumping frequency.

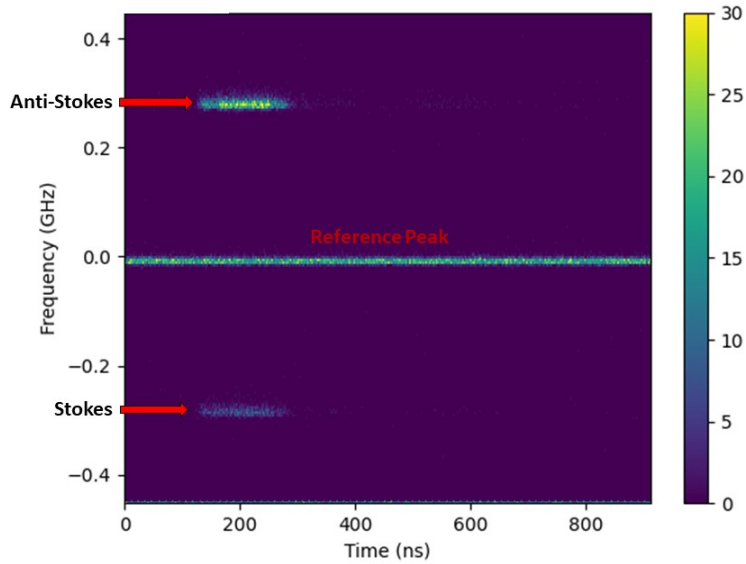


Figure 3.9: The intensity of the inelastically scattered photon frequency shift over time for one position on the sample. The bright spots indicate the BLS signal intensity. The bright line in the center (at $f=0$) is the reference beam, and the red arrow points to the signal from the spin wave pulse.

Fig. 3.9 shows the full raw time-resolved data set for the same location as Fig. 3.8, and Fig. 3.10 is a demonstration of how figures like 3.8 are combined to make a time-resolved dataset shown in Fig. 3.9. In Fig. 3.9 the brightness scale indicates the intensity of photon counts. Figs. 3.8 and 3.9 and were measured at the same position under the same conditions, but Fig. 3.9 shows the intensity of the frequency shift over time instead of the frequency shift at one specific time (Fig. 3.8). The bright beam in the middle is due to the reference beam. The bright patches below and above the reference beams, at -4.25 GHz and 4.25 GHz, are the counts from the spin wave pulse detected at the Stokes and anti-Stokes frequency shifts.

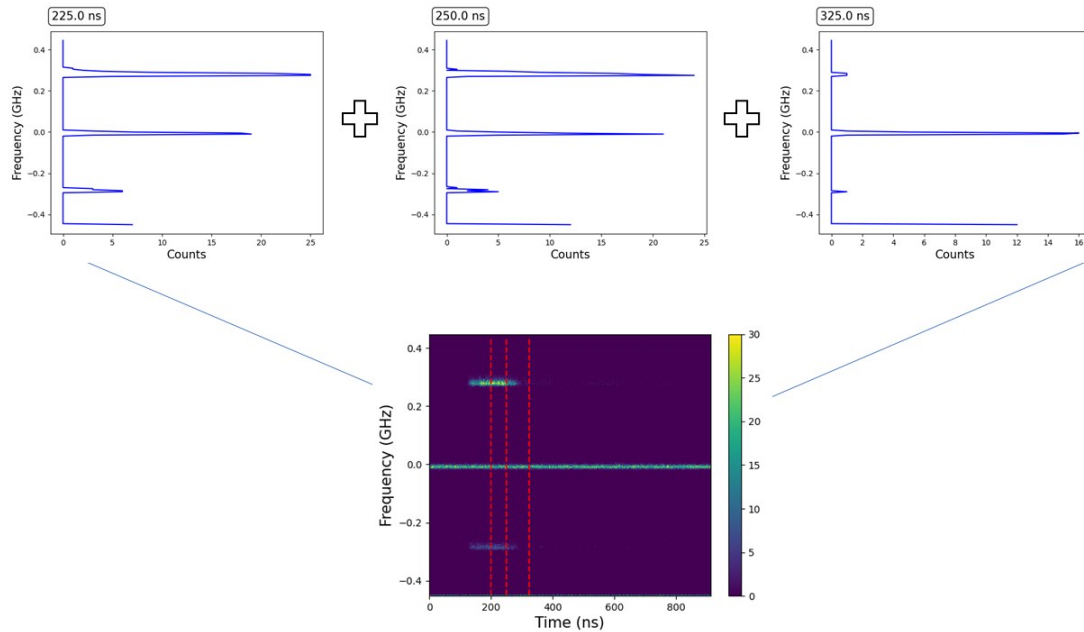


Figure 3.10: A visual representation of how the counts versus frequency time graphs are combined to create the frequency versus time graphs. The red dashed lines correspond with the selected times for the counts versus frequency graphs above.

The spin wave pulse is obtained at each position by taking the integral of the Stokes or anti-Stokes regions, as shown in Fig. 3.11. Choosing to integrate the Stoke or anti-Stokes region does not matter, but choosing whichever has the highest counts is better for data analysis. Repeating this integration process for an intensity versus frequency and time graph at every position results in multiple counts versus time, or pulse, graphs. Then combining all the pulses will result in a Fig. 3.12 for tracking the intensity of the spin wave pulse as it travels in the magnonic crystal. Fig. 3.13 demonstrates in more detail how combining the pulse graphs creates an intensity versus position and time graph, like Fig. 3.12.

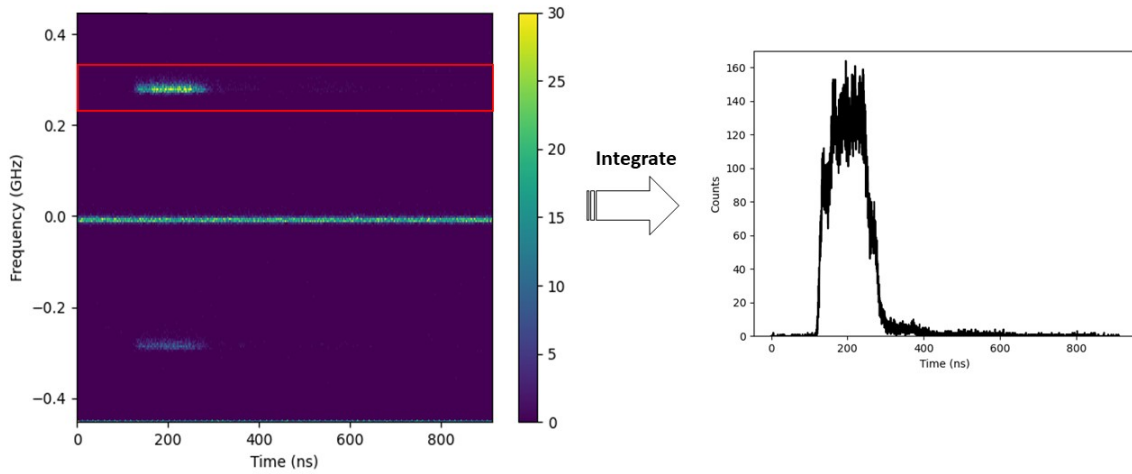


Figure 3.11: Integrating the signal over the frequency range indicated by the red box leads to a plot of the integrated BLS counts versus time, spin wave pulse, at one position.

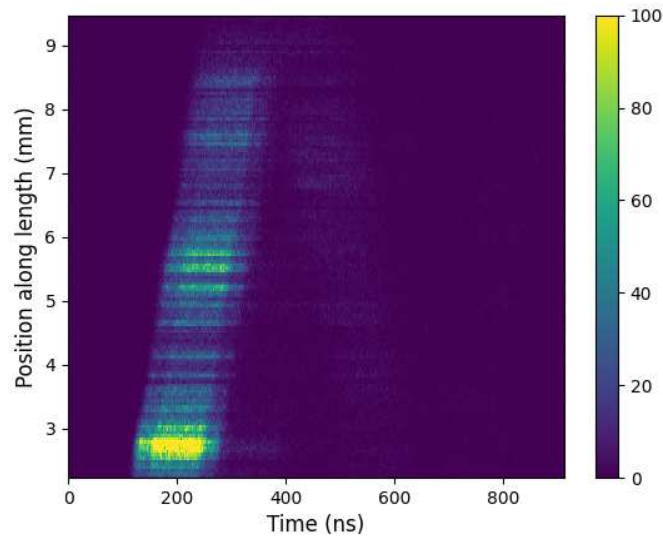


Figure 3.12: Tracking the intensity of the spin wave, at the BP frequency, as it travels down the sample length (along x) over time. When there are brighter spots, there are more counts and the spin wave has a higher intensity. Here the spin wave pulse is shown at the center of the sample width-wise ($y = 11.92$ mm).

Fig. 3.12 shows the intensity of the spin wave pulse as it travels down the center of the magnonic crystal over time. The bright spots indicate there is a spin wave present, while at the less bright spots there might be a less intense spin wave. Fig. 3.12 shows a faint triangle pattern for the spin wave that travels down and is then reflected back along the length of magnonic crystal over time. The bright left side of the triangle shows the main spin wave pulse traveling from the antenna in the positive x direction down the length of the sample. The faint right side of the triangle is due to the spin waves that have reflected off the end of the crystal and they are traveling in the negative x direction back to the front. These types of intensity versus position and time plots are made to observe spin waves traveling down the length or the width of the magnonic crystal.

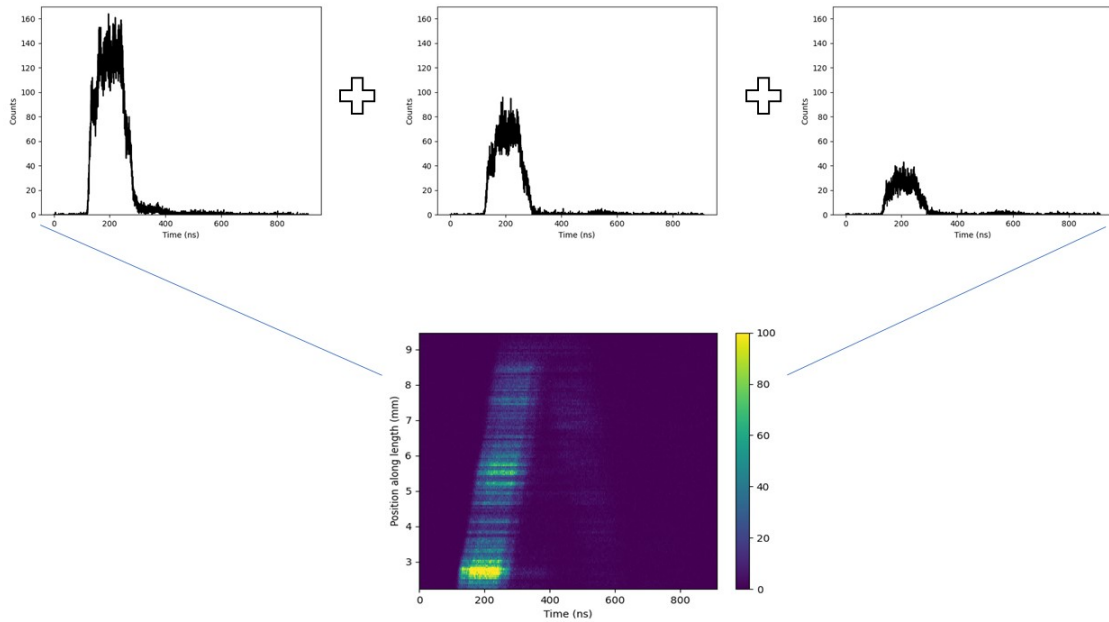


Figure 3.13: A visual representation of how the counts versus time graphs are combined to create the plot of intensity versus position and time graphs.

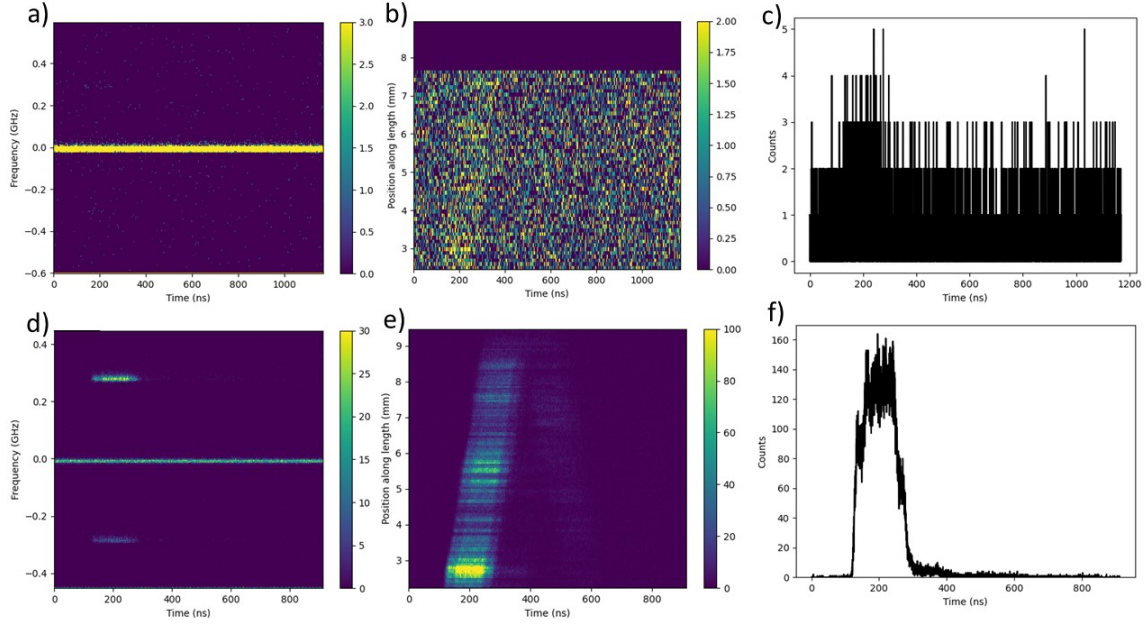


Figure 3.14: TR-BLS measurements made on a 1D magnonic crystal. a), b), and c) were obtained at a driving frequency of 4.41 GHz and $H = 900$ Oe and d), e) and f) at 4.25 GHz and $H = 855$ Oe. There were software interruptions and resulted in no counts for $x > 7.5$ mm for b).

Fig. 3.14 shows the preliminary TR-BLS dataset taken by me. The overall measurement time took a couple of hours and resulted in data with fewer counts. The measurements were made in a forward scattering surface wave configuration. The applied magnetic field was $H = 900$ Oe with a 4.41 GHz driving frequency. The data processing procedure described above was applied and resulted in Figs. 3.14 a), b), and c). While taking measurements, there was a software interruption, which is why no counts were recorded for $x > 7.5$ mm in Fig. 3.14 b).

Even though the counts are low, the spin wave pulse is visible and the group velocity of the pulse can still be determined. The group velocity can be calculated by taking a rough estimate of the slope in the intensity versus position and time graph (Fig. 3.14 b).

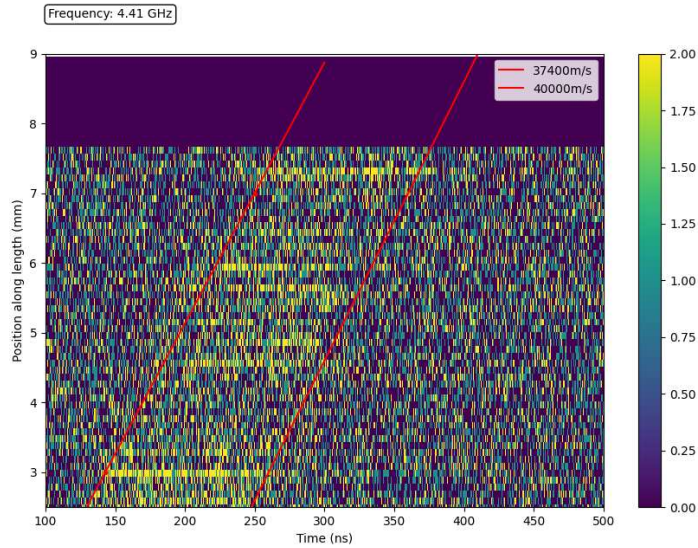


Figure 3.15: Illustration of the manual calculation of the group velocity using the preliminary intensity versus position and time data. This is done by finding the general slope of the brighter region (red lines). The group velocities are given in the legend.

The group velocity found falls in the estimated range for a spin wave in a 1D YIG magnonic crystal (40 km/s) [2]. The estimated group velocity is around 39000 m/s and the experimental group velocity for a similar driving frequency (BG2), calculated in section 4.5.3, is 38000 m/s.

To get a more exact group velocity and details about the pulse shape, measurements need to run longer to collect more photon counts. A fellow group member, M. Swyt, ran measurements with a longer dwell time per point at the identified frequencies from the transmission profile (table 3.1) to collect more counts. The set up was also in a forward scattering surface wave configuration with an applied magnetic field of 855 Oe. This dataset has a better signal to noise ratio and the pulse shape is easier to identify as seen in the bottom row of Fig. 3.14.

With the higher count dataset, the pulse shape is easier to identify, and the group velocity can be determined by tracking the pulse as it travels down the sample using more sophisticated techniques instead of by estimating the slope in the position versus time graph. The dataset with higher counts was used in the beginning of this section to demonstrate the data processing procedure. All further analysis done in this thesis also focuses on the higher count dataset.

Chapter 4

Analysis

4.1 Introduction

This section discusses the different methods used to analyze the pulse shape and the group velocity, as well as the result of the analysis. The stripline antenna attached to the sample excites a spin wave down the length of the sample (Fig. 3.1). By using cross-correlation, a method commonly used for signal processing, the spin wave pulse speed and shape can be tracked as it travels down the sample.

First, how the pulse propagates in the sample will be explained. Then a detailed review of the cross-correlation method and how it is used will be described. Lastly, the average group velocity of the pulse and changes to the pulse characteristics will be discussed. Most of the analysis on the pulse shape will focus on data obtained at the frequencies corresponding the band pass (BP) and the first two band gaps (BG1, BG2) (Fig. 3.2). Measurements were also made at BG3, however, the counts were low and it was difficult to identify features in the pulse.

4.2 Pulse Selection

To analyze the group velocity and the shape of the spin wave pulses measured by the TR-BLS, a single reference pulse and a width-averaged reference pulse were chosen and compared to pulses in the 1D magnonic crystal at different locations. Fig. 4.1 shows a diagram of the 1D magnonic crystal with key measurement positions identified and the exact locations are listed in table 4.1.

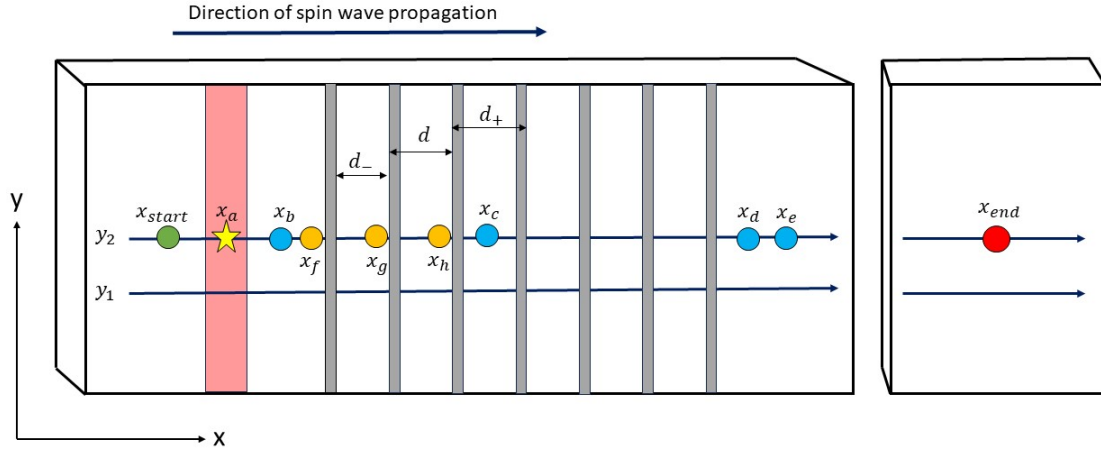


Figure 4.1: A schematic of various key locations along the 1D magnonic crystal referenced in the analysis and a list of the exact positions can be found in table 4.1. The TR-BLS scan range extends from x_{start} to x_{end} and across the full width (y-direction) of the crystal. The yellow star indicates the position for the single reference pulse. The width-average reference pulse was taken by averaging all the pulses along the red bar region. The grey bars are the grooves. This diagram is not to scale.

Table 4.1: A list of key positions for the BP, with an uncertainty of 0.01 mm, corresponding to Fig. 4.1. The measurements start 1 mm from the antenna.

Name	Position
x_{start}	2.25 mm
x_{stop}	9.5 mm
x_a	2.65 mm
x_b	2.8 mm
x_c	3.64 mm
x_d	4.43 mm
x_e	4.48 mm
x_f	2.95 mm
x_g	3.24 mm
x_h	3.54 mm
y_1	11.24 mm
y_2	11.92 mm
d_-	250 μm
d	275 μm
d_+	300 μm

The pulse at the center, width-wise, of the sample with the maximum number of counts was used as the single reference pulse ($x = x_a$, $y = y_2$). The width-averaged reference pulse is constructed by taking all the pulses along the width of the crystal and averaging the pulse counts. For the BP, the width-averaged pulse was constructed by averaging the pulses along at the same x position, x_a , as the single reference pulse. For all frequencies (BP, BG1, BG2, and BG3), the width-averaged reference pulse counts were scaled up to match the number of counts of the single reference pulse. This step is important for later analysis using cross-correlation. Fig. 4.1 shows the location of the single reference pulse, the star, and the width-averaged reference pulse, the red

stripe. For BG1, BG2, and BG3 the highest number of counts for the single reference pulse and the width-averaged reference pulse are located at different x positions than BP, (Fig. 4.1).

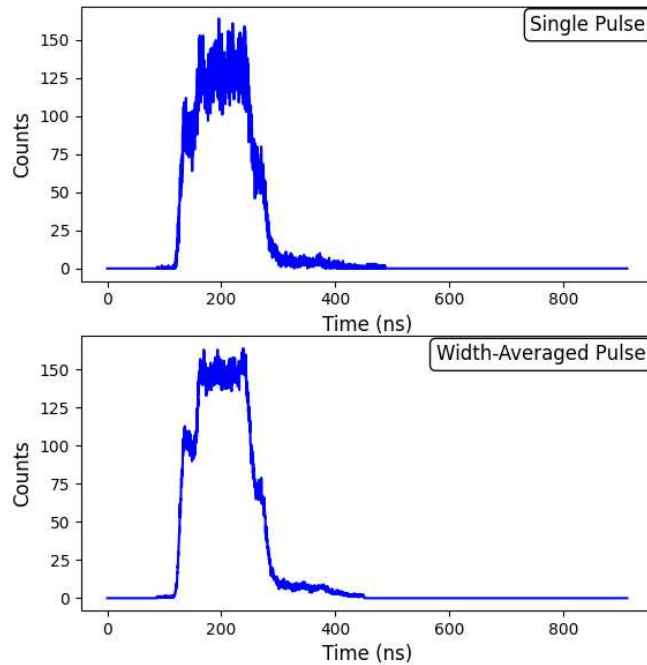


Figure 4.2: Diagram of the single reference pulse and the width-averaged reference pulse at BP. The pulses were truncated to include only the main pulse and eliminate the pulse reflected back from the end of the crystal.

A comparison of the two reference pulses can be seen in Fig. 4.2. The pulses were trimmed to exclude the counts from the reflection of the pulse off the end of the sample. The group velocity analysis was done using both the single reference pulse and the width-averaged reference pulse and the results were compared. Throughout this thesis the single reference pulse will be referred to as the “single pulse” and the width-averaged reference pulse will be referred to as the “average pulse.”

4.3 Cross-Correlation

Cross-correlation is a common method used in signal processing because it can be used to determine how similar two signals are to each other. A cross-correlation of two functions is done by sliding one of the functions over time, and then calculating the integral of the product of the two functions for each lag time. The cross-correlation of two functions, $f(t)$ and $g(t)$, is given by [25].

$$(f * g)(\tau) = \int_{-\infty}^{\infty} \overline{f(t)}g(t + \tau)dt \quad (4.1)$$

$$(f * g)(\tau) = \int_{-\infty}^{\infty} \overline{f(t - \tau)}g(t)dt \quad (4.2)$$

The $*$ denotes convolution. $\overline{f(t)}$ denotes the complex conjugate of $f(t)$, and τ is the displacement, or the lag time, between the functions. The integral for cross-correlation can be taken over an infinite time range or over a finite time range. The cross-correlation range for the TR-BLS signals data was taken over the signal time. The range for the normalized cross-correlation amplitude is from -1 to 1. Where 1 indicates perfect cross-correlation and -1 indicates perfect anti cross-correlation. When there is no correlation, the value is 0 [26].

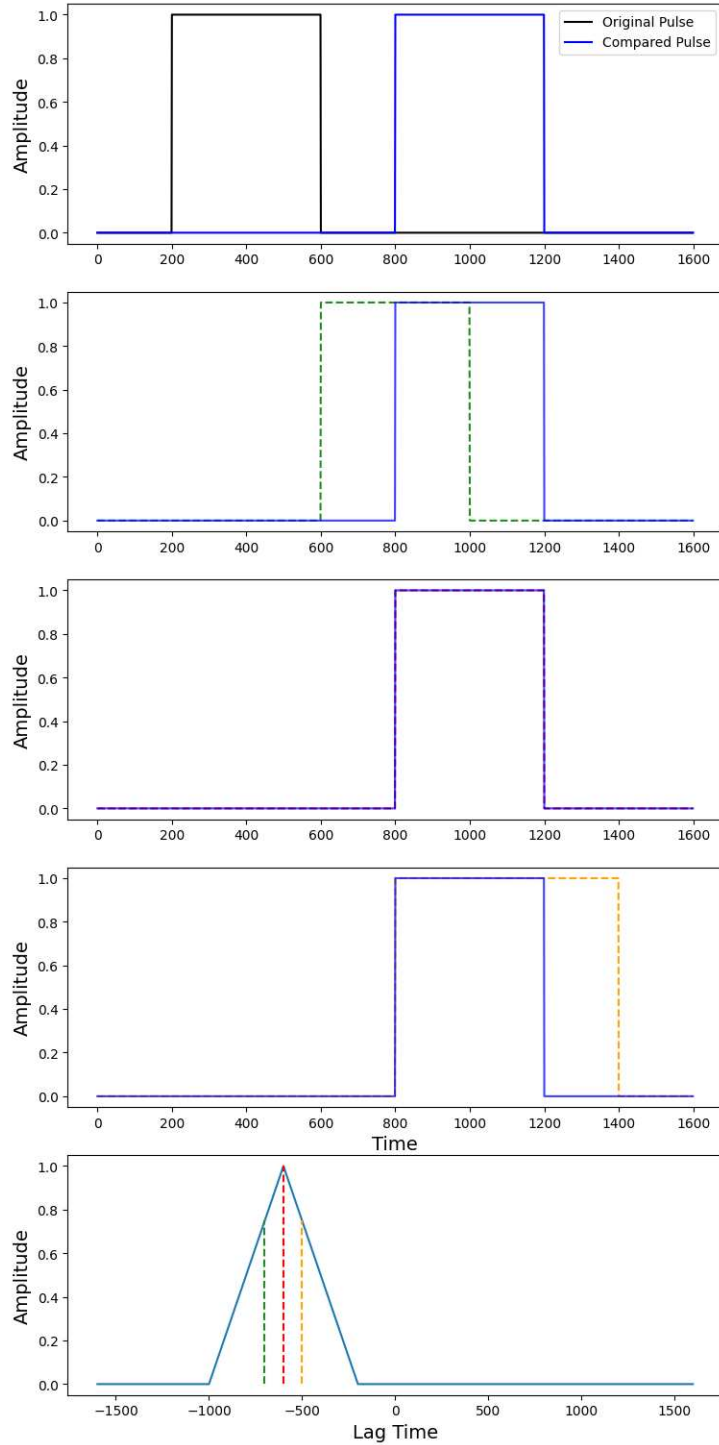


Figure 4.3: Diagram of the cross-correlation process. The first panel shows the original pulse, black line, and the compared pulse, blue line, compared, for a case where the correlation is zero. The next three panels show the corresponding cross-correlation values as the original pulse is shifted. The last panel are the results of the cross-correlation for the two pulses. The green, red, and orange dotted lines in the cross-correlation value correspond with the shifted pulses colors.

An example of a cross-correlation is shown in Fig. 4.3. When the original function, the black function, and the second function, the blue function, do not overlap at all, the cross-correlation value is 0 (top panel of Fig. 4.3). As the original function is shifted to the right and begins to overlap with the second function, the cross-correlation value increases. When the two functions are slightly overlapped, as seen with the green and orange dotted lines, the cross-correlation value is greater than 0, but not 1. When the two functions overlap perfectly, the cross-correlation value is 1. The time at the maximum cross-correlation value is called the lag time, τ_{max} . The maximum amplitude, in Fig. 4.3 is found to be at a lag time of around -600 s. Visually, this can be double checked by shifting one pulse with respect to the other by τ_{max} and the pulses should then overlap. The sign of τ_{max} for this case is not important. It can be positive or negative depending on which function is being displaced. If the second function, the blue function, was the function being shifted, then the lag time would be $+600$ s, instead of -600 s.

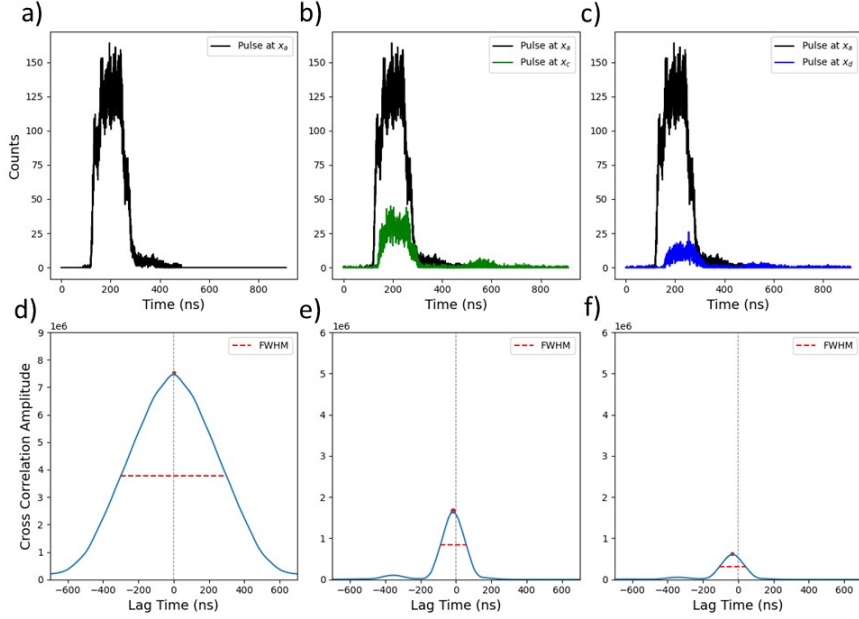


Figure 4.4: An example of the cross-correlation for the pulses. The top row are the pulses compared to each other and the bottom row is the corresponding cross-correlation of the pulses. d) is the autocorrelation of the single pulse in a). e) and f) are the cross-correlation of the single pulse with spin waves pulses at different locations, b) and c). The amplitude of the cross-correlation, e) and f), has been scaled to show how the amplitude changes when the pulse counts or shape changes, as compared to the autocorrelation amplitude in d). However, the cross-correlation amplitude scale is not normalized to 1. The red circle indicates the maximum cross-correlation amplitude (τ_{max}) and the grey line dashed line is centered at lag time 0 ns. The red dashed line is the full width half max (FWHM) of the cross-correlation.

The cross-correlation method is applied to the reference pulse and pulses at different locations on the magnonic crystal. Fig. 4.4 d), e) and f) are examples of how the lag time and the full width half max (FWHM) can be obtained from the cross-correlation of the TR-BLS data. Fig. 4.4 d) is the autocorrelation of the single pulse, where an autocorrelation is the cross-correlation of a function with itself. An autocorrelation will have the maximum cross-correlation amplitude as compared to the cross-correlation of the reference pulse with a pulse at any other location. If the pulse does not have the same shape or has fewer counts than the reference pulse, then the amplitude of the cross-correlation will be smaller. For example, the autocorrelation amplitude shown in Fig. 4.4 d) is larger than the cross-correlation amplitudes from Figs. 4.4 e) and f). The cross-correlation amplitude in Figs. 4.4 e) and f) are shown on a different scale than the autocorrelation amplitude,

Fig. 4.4 d). The peak of the cross-correlation amplitudes in Figs. 4.4 d), e), and f), indicated by the red point, are greater than 1 because the amplitude is not normalized.

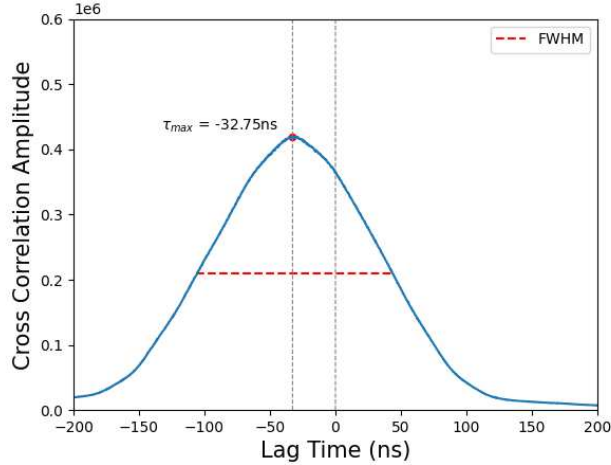


Figure 4.5: A zoomed in version of the cross-correlation of pulses at x_a and x_d from the cross-correlation in figure 4.4 f) to show the lag time.

The lag time associated with the maximum value of the cross-correlation (τ_{max}) gives the pulse time shift for a given position, which can be used to determine the group velocity of the spin wave pulse. Fig. 4.5 is a zoomed in version for Fig. 4.4 f). The lag time of the autocorrelation is 0 ns. The time between 0 ns, shown by the grey dashed line, and the peak of the cross-correlation amplitude, the red point, is the lag time between the pulse and the reference pulse. To find the group velocity down the center of the sample, the single pulse, denoted by the star in Fig. 4.1 was used as the reference pulse and then cross-correlated with pulses at position $x_{a,b,c,d,etc}$. Then the lag time for each cross-correlation is plotted as a function of position, and the group velocity down the length of the sample (x direction) at width position y_2 is obtained from the slope ($v_g = 1/\text{slope}$). This will be discussed in more detail in section 4.5.1.

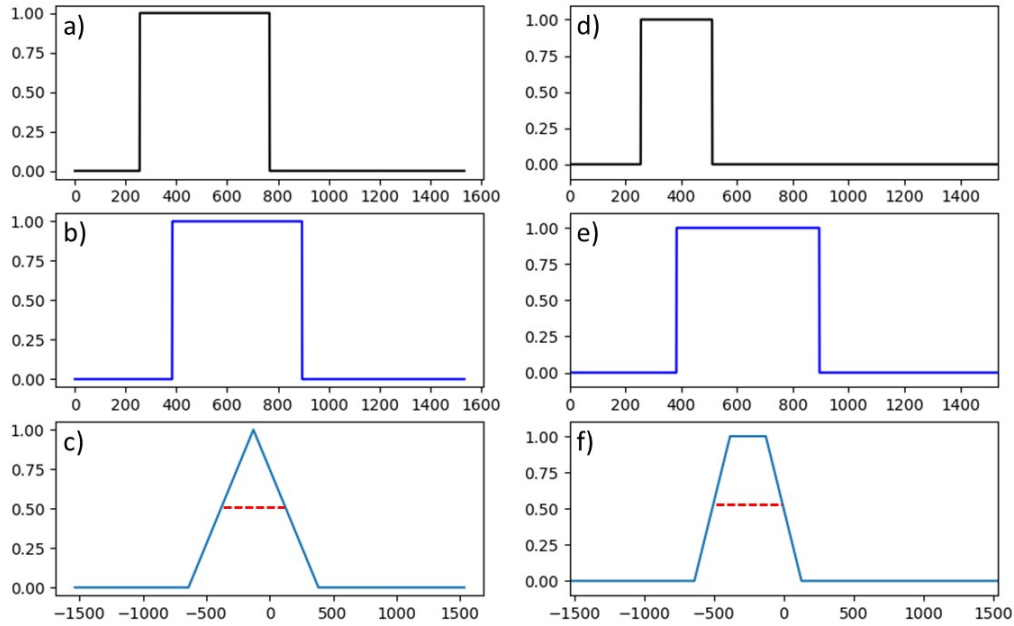


Figure 4.6: Example of the width of the cross-correlation amplitude changing based on pulse width. c) is the cross-correlation amplitude of pulses in the first column and f) is the cross-correlation amplitude of the pulses in the second column. Pulse a) duration (550 ns) is less than the duration for pulse d) (275 ns). The resulting cross-correlation FWHM, marked in red for c) is 530 ns and the FWHM for f) is 450 ns.

Fig. 4.6 illustrates how changes in the cross-correlation FWHM indicates pulse shape changes. The pulse duration of Fig. 4.6 a) is 550 ns and is the same duration as the second pulse, the blue function (Fig. 4.6 b). Fig. 4.6 c) shows the resulting cross-correlation with a FWHM of 530 ns. The resulting FWHM of the cross-correlation for pulse in Fig. 4.6 d) and Fig. 4.6 e), where Fig. 4.6 e) is the same duration as the pulse in Fig. 4.6 b), is 450 ns. When the pulse duration for the reference pulse decreases, the cross-correlation FWHM also decreases. By looking at how the FWHM of the cross-correlation changes from the autocorrelation FWHM, the changes in pulse shape in the magnonic crystal can be quantified. The FWHM for the magnonic crystal pulses are shown by the red dashed line in Figs. 4.6 c) and f).

4.4 Pulse Propagation

4.4.1 Pulse Along the Width

In this experiment the antenna is positioned such that the spin waves should travel along length (x direction), and the arrival times should be constant along the width (y direction) for a given x (Fig. 3.1). The average of the pulse speed should be nonzero only along x. This can be verified in a few ways. First, Fig. 4.7 shows the pulse intensity across the width. Unlike Fig. 3.12 where the pulse position changes over time, in Fig. 4.7 the pulse is concentrated at one time range for all widths where the pulse is visible.

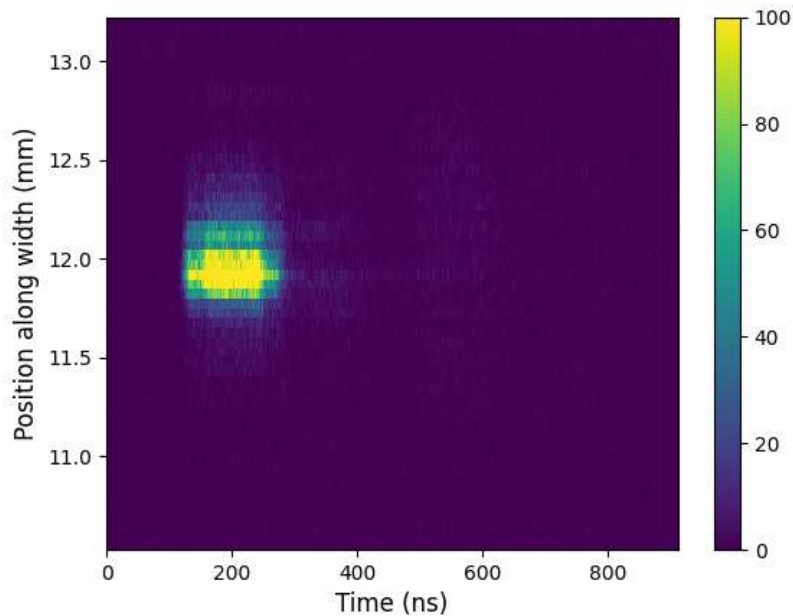


Figure 4.7: Tracking the pulse intensity across the width of the sample at x_b with a driving frequency BP.

Fig. 4.8 shows the lag times versus y obtained from the cross-correlation of the pulses along the width at the position x_c with the single pulse. As shown in Fig. 4.8, the lag times between the single pulse and the pulses compared at different y positions were close to 0 ns, as expected. Along the edges of the sample the lag time increases. This could be due to the lower counts, so the lag times from the cross-correlations are less reliable.

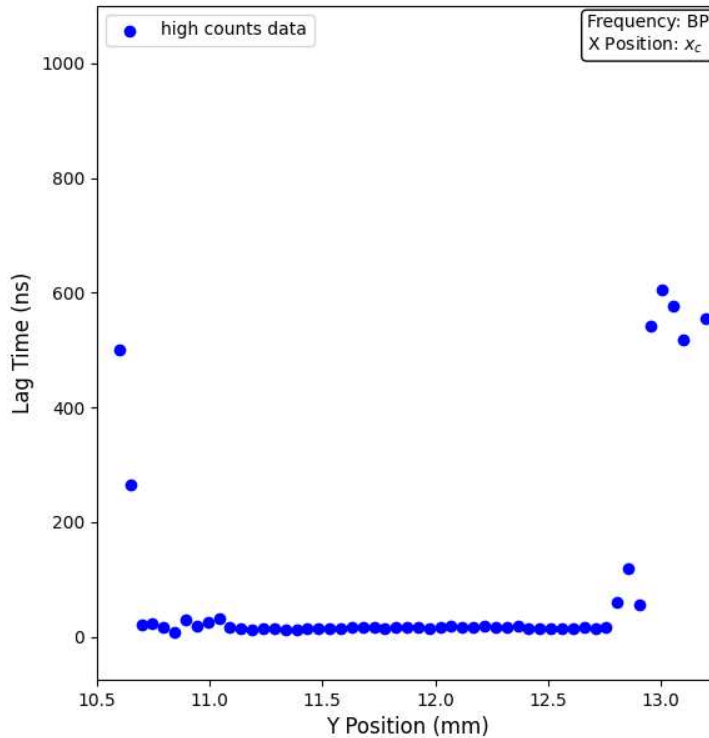


Figure 4.8: The lag time for the cross-Correlation for every position along the width at driving frequency BP.

The FWHMs from the cross-correlations of the pulses across the width were also examined (Fig. 4.9). It is expected as the pulses travel there will be some pulse spreading. Along the width the pulses do not spread or change shape. Fig. 4.9 shows that at the BP frequency the FWHM is relatively constant across the sample width with the average FWHM value of 150 ns. The blue points in Fig. 4.9 are data points with high counts, that correspond to values within 10 % of the peak autocorrelation amplitude. The orange points have a lower cross-correlation amplitude. The pulses along the edges of the crystal have lower counts and this affects the cross-correlation shape and leads to less consistent FWHMs values. The pulse intensity plot (Fig. 4.7) and lag times plot (Fig. 4.8) shows that the pulse does not travel along the width, and Fig. 4.9 verifies that there is minimal spreading, as expected.

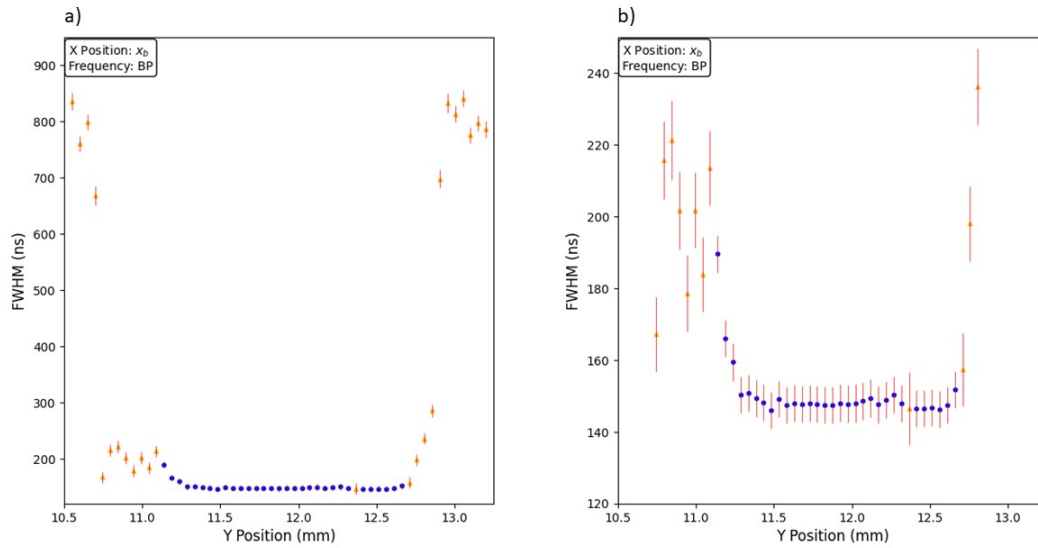


Figure 4.9: a) is the FWHM of the cross correlation amplitude across the width of the sample for a driving frequency of BP. b) is the zoomed in version of a). The blue and orange points are data points with higher and lower counts respectively.

4.4.2 Diamond Pattern

Next the pulse propagation along the length of the sample will be analyzed, however, before this is done it is important to note that the TR-BLS data shows that the pulse propagation is complicated in a YIG strip. When using the TR-BLS data to track the pulse traveling down the sample, a diamond pattern emerges as seen in Fig. 4.10.

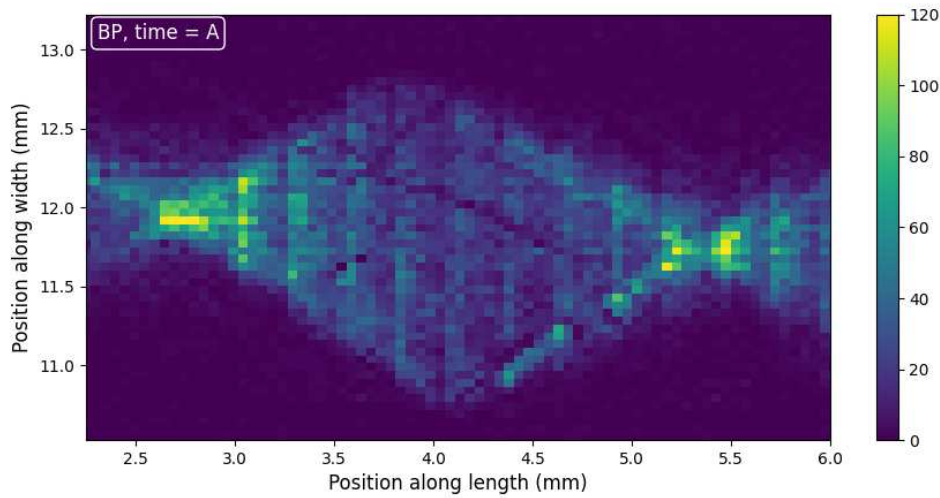


Figure 4.10: TR-BLS data for the pulse traveling down the sample, at time = A (200 ns), where a diamond shape appears. This is due to different modes simultaneously excited by the antenna.

One might think the diamond pattern is due to the pulse moving in a diagonal direction and reflecting off of the sides of the sample. However, in the previous section it was established that the pulse does not propagate along the width. Therefore, the diamond pattern must be caused by something else. It turns out the diamond pattern is a result of width-quantized spin wave modes excited by the antenna. The interference of these width-quantized spin wave modes leads to a spatial pattern and a periodic self-focusing effect of the propagation of spin waves. The diamond pattern will form even in unpatterned YIG films and it is not due to the periodic modulation in the magnonic crystal [27,28].

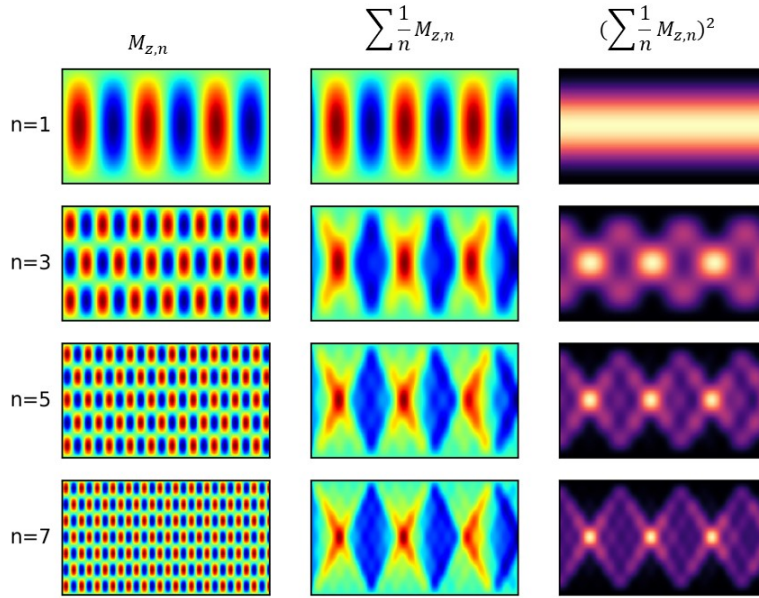


Figure 4.11: Calculations to illustrate the formation of the diamond pattern from lower modes due to the interference of the different width-quantized modes simultaneously excited by the antenna. The first column shows the standing wave pattern of the out-of-plane magnetization M_z . The second column shows the cumulative sum of the magnetization for each mode and each mode with a phase shift of $\pi/2$. The third column is intensity, proportional to the BLS signal, and is the total magnetization integrated over one full period. Each panel is a snapshot at an instant in time.

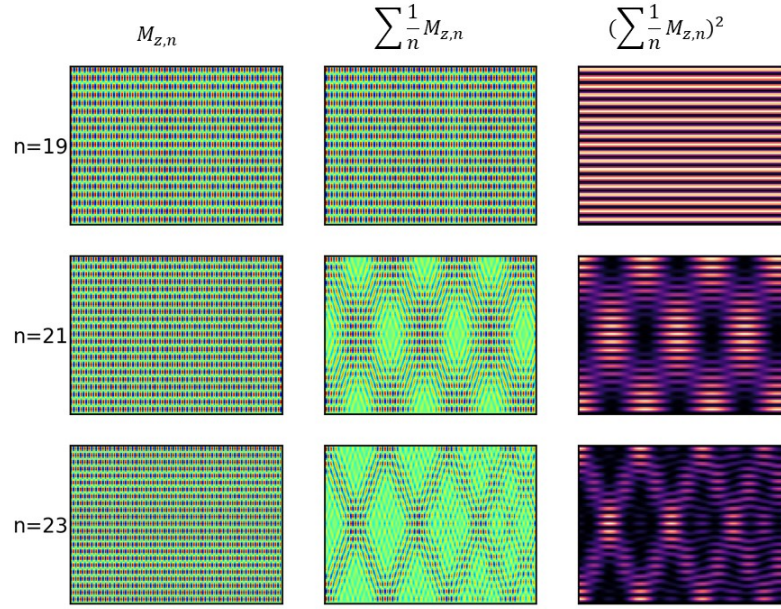


Figure 4.12: Calculation to simulate the diamond pattern formation only using higher modes due to the interference of the different width-quantized modes simultaneously excited by the antenna. The first column shows the standing wave pattern of the out-of-plane magnetization M_z . The second column shows the cumulative sum of the magnetization for each mode and each mode with a phase shift of $\pi/2$. The third column is intensity, proportional to the BLS signal, and is the total magnetization integrated over one full period. Each panel is a snapshot at an instant in time.

The wavevectors that are allowed along the length of the sample (x direction) are continuous. However, since the width of the sample is small, the wavevectors in the y direction are quantized. Across the width, the magnetization goes to 0. This leads to the out-of-plane magnetization (M_z) across the width to act like standing waves, as shown in the first column of Fig. 4.11, starting with the $n = 1$ mode. Figs. 4.11 and 4.12 are calculations of the low and high mode interference that results in a diamond pattern.

Since a stripline antenna is used to excite the spin waves, multiple surface spin waves modes are excited simultaneously, and it is not possible to select a specific wavevector to propagate. Only the modes with odd n ($n = 1,3,5, \dots$) are allowed. The modes with even n ($n = 2,4,6, \dots$) have odd symmetry. So, when the magnetization for the modes with even n are summed, the magnetization will cancel out and the even modes are not excited by the antenna. Each mode is excited with a relative magnetization amplitude of $1/n$ [27]. So, the $n = 1$ mode is responsible for the majority of

the pulse dynamics like the average speed and shape. Interference of the $n = 1$ mode with the $n = 3, 5, 7, \dots$ modes leads to the observed diamond pattern. The width quantized modes, k_n

$$k_n = \frac{n\pi}{w} \quad (4.3)$$

are calculated using equation 4.3 where w is the width of the sample, 2.25 mm, and n is the mode number. Each mode has a different k_n . The standing wave pattern for the odd modes are shown in the first column of Fig. 4.11 and 4.12. Red is the maximum intensity of M_z and blue is the minimum. The magnetization for each n mode, m_n ,

$$m_n(x, y) \propto \frac{1}{n} \sin\left(\frac{n\pi}{l}y\right) e^{i(k_x x + \phi)} \quad (4.4)$$

where l is the width of the sample, k_x is the wavevector in the x direction, and ϕ is the phase.

The third column in Fig. 4.11 and 4.12 is the amplitude of the spin wave, or intensity (I),

$$I \propto \left(\sum m_n\right)^2 \quad (4.5)$$

which is measured by the BLS. The intensity is obtained by integrating the total magnetization over one period. The total magnetization is the cumulative sum of M_z for different wavevectors of each mode. Another element of the M_z with a phase shift of $\pi/2$ for each mode is included in the sum to simulate the dynamics of the plane wave moving. The resulting sum of each mode is shown in the second column of Fig. 4.11 and 4.12 starting at $n = 1$ for the first row and each subsequent row adds an additional mode.

The filled in diamond pattern appears with contribution to the intensity calculations from the lower modes. As shown in Fig. 4.12, when only the intensity for the higher modes is calculated, the diamond pattern still exists, but it is only the outline and not filled in. In section 4.6.2 the diamond patterns from the calculations will be compared to the images obtained from the data set. For now, the important takeaway is that the amplitude variation as a function of x is not expected to follow a simple exponential decay pattern.

4.5 Group Velocity

4.5.1 Group Velocity using Cross-Correlation

The group velocity down the center of the sample is found by taking the slope of the lag time from the cross-correlation plotted for every position. Fig. 4.13 uses the single pulse, star on Fig. 4.1, as the reference pulse for the cross-correlation.

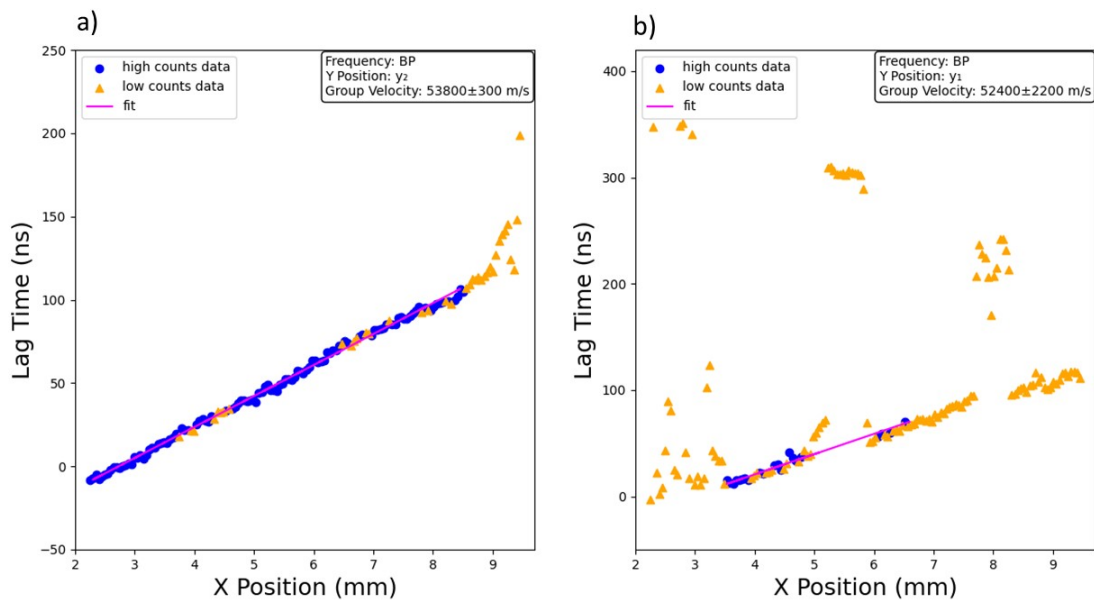


Figure 4.13: Lag time as a function of x for the BP driving frequency. The blue points have a higher cross-correlation amplitude and the orange points have a lower cross-correlation amplitude. The group velocity and the associated uncertainty are obtained from linear least squares fits. Only the blue points were used for fitting, because they have higher counts. a) is the the group velocity down the length at y_2 and b) is the group velocity at y_1

Fig. 4.13 shows the extracted lag times as a function of the position along the sample length (x direction) for two different y positions (y_1 and y_2). The points in Fig. 4.13 are categorized as high counts data (blue points) and low counts data (orange points) based on their cross-correlation amplitudes. If the cross-correlation amplitude fell within 10% of the autocorrelation amplitude, then the pulse was labeled as a high counts data. If it fell out of this range, then it was considered low counts data.

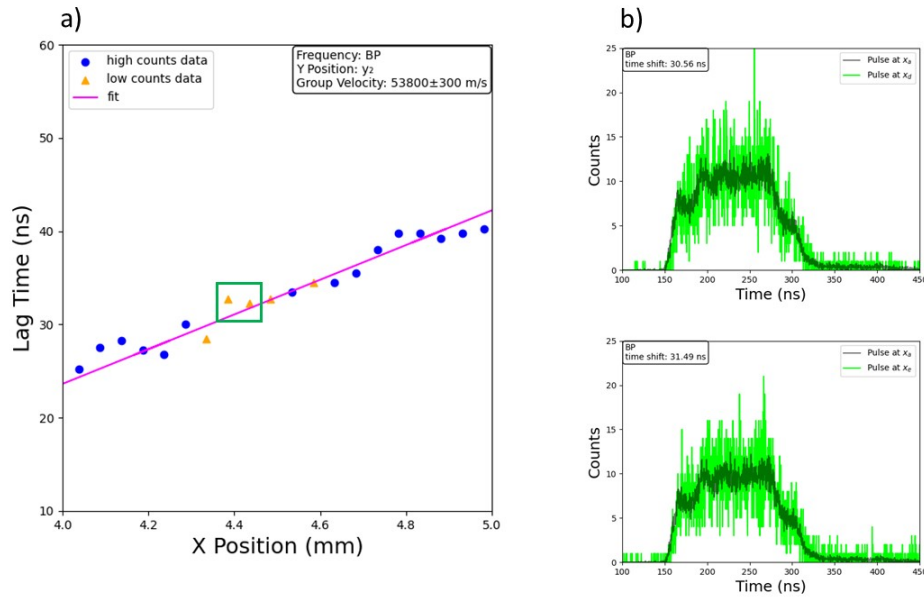


Figure 4.14: a) is a zoomed in version of figure 4.13 a). b) are the two pulses highlighted by the green box in a). The reference pulse (black pulse) has been scaled and shifted by the lag time to match the green pulse.

The positions with low counts could be caused by destructive interference off the grooves or be at particular positions in the diamond pattern that has low intensity counts. Fig. 4.14, a zoomed-in version of Fig. 4.13, demonstrates why the two points are categorized into high counts data or low counts data. Fig. 4.14 b) are the pulses compared to the reference pulse in the green box for Fig. 4.14 a). The reference pulse has been scaled and shifted by the lag time to compare with the green pulses at positions x_d and x_e . When compared to the reference pulse, the green pulses' counts are lower and the shape is less defined. These pulses have more inconsistent cross-correlation value. So, when the group velocity is calculated by the curve fitting, pink line in Fig. 4.13, only the high counts data are used. Fig. 4.13 a) show the group velocity at position y_2 , 53800 ± 300 m/s, down the center of the crystal. Fig. 4.13 b) is the group velocity at position y_1 , 52400 ± 2200 m/s. The group velocities are the same within the uncertainty, which is expected.

To examine the group velocity in the entire sample, the method described above is repeated for every position along the width. Both the single pulse and the average pulse are used as the reference pulses in the cross-correlation to verify the group velocity is consistent. Fig. 4.15 shows

the group velocity for every width position. Fig. 4.15 a) show the group velocities using the single pulse as the reference pulse, and Fig. 4.15 b) are the group velocities using the average pulse as the reference pulse. The red dashed line is the average group velocity. Only points with a sufficiently large cross-correlation amplitude (high count data) are used to calculate the group velocity. As a result, some regions are omitted from the analysis.

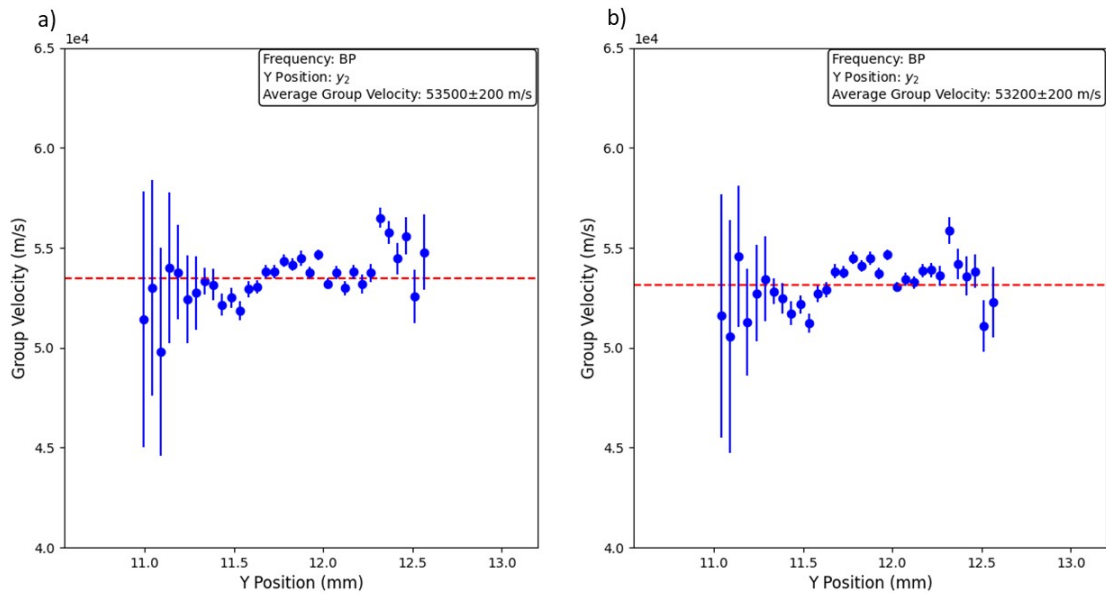


Figure 4.15: The group velocities at the BP for every width position where in a) the single pulse was used as the reference pulse to calculate the velocities, and in b) the average pulse was used as the reference pulse to calculate the group velocities.

The average group velocities in the magnonic crystal obtained using the single pulse and the average pulse as the reference pulse are within the same uncertainty. At the BP frequency, using the single reference pulse results in an average group velocity of 53500 ± 200 m/s. The average pulse results in an average group velocity of 53200 ± 200 m/s.

The cross-correlation method is repeated to obtain the group velocities for BG1, BG2, and BG3 frequencies. The results are summarized in table 4.2.

4.5.2 Group Velocity using Dispersion Relation

The expected group velocities can be obtained from the dispersion relations calculated for a YIG film using the material parameters for YIG, sample thickness, and width. Fig. 4.16 shows the width-quantized dispersion relations calculated for modes $n = 1$ to $n = 45$, where the $n = 1$ mode has the highest amplitude for the intensity for a given wavevector, hence the $n = 1$ group velocity will be the dominant velocity of the spin wave pulse. These dispersion relations were calculated by M. Swyt using the theory in Kalinikos 1986 [29].

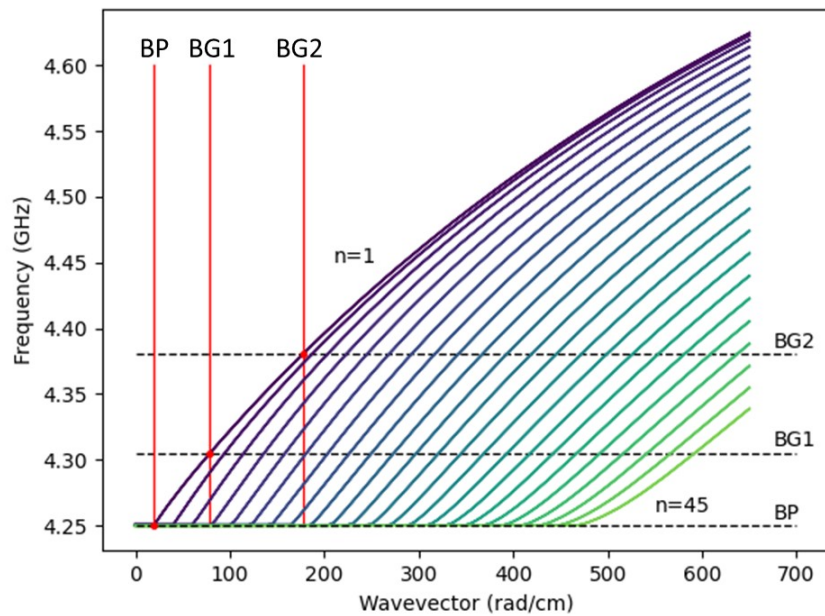


Figure 4.16: The dispersion relation for modes $n = 1$ to $n = 45$, where n is the index for the width quantized modes. Only the modes with odd n are shown. The red points mark the wavevectors corresponding with $n = 1$ for each frequency. (BP wavevector = 19 rad/cm, BG1 wavevector = 79 rad/cm, BG2 wavevector = 176 rad/cm).

To find the group velocity, first the corresponding wavevector from the intersection of the driving frequency with the $n = 1$ line on the dispersion relation is identified. In Fig. 4.16 this is shown with a red dot. For BP the wave vector is 19 rad/cm, the wavevector for BG1 is 79 rad/cm, and the wavevector for BG2 is 176 rad/cm.

Next, the slope of the dispersion relation, also the group velocity $v_g = \frac{d\omega}{dk}$, for each mode is plotted (Fig. 4.17). In Fig. 4.17, the lowest mode ($n = 1$) starts on the far left. The group velocity for a particular mode is determined by finding the intersection of the identified wavevectors from Fig. 4.16 with the group velocity line. This is shown in Fig. 4.17 with the red line at the wavevectors and a red dot at the intersection. For BP the group velocity is 64800 ± 1000 m/s. BG1 group velocity is 52200 ± 1000 m/s and BG2 group velocity is 44000 ± 1000 m/s.

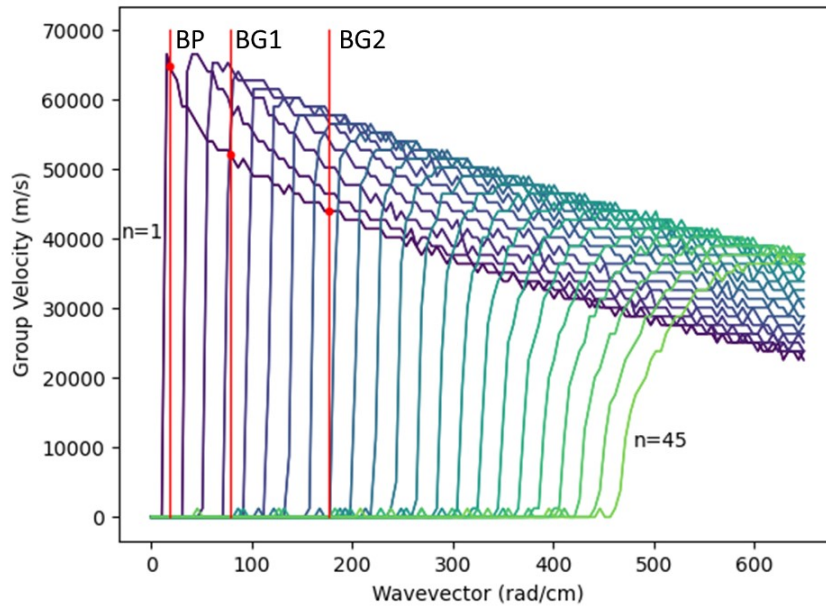


Figure 4.17: The group velocity for modes $n = 1$ to $n = 45$, where n is the index for the width quantized modes. Only the modes with odd n are shown. Using the wavevectors identified in Fig. 4.16 the corresponding group velocities, marked by red points, are extracted. (BP group velocity = 64800 m/s, BG1 group velocity = 52200 m/s, BG2 group velocity = 44000 m/s).

As discussed in the explanation of the diamond pattern, multiple modes are excited with the stripline antenna. Each mode has a different wavevector and therefore a different group velocity. The effects of the different mode group velocities will be further discussed in the pulse shape analysis section.

4.5.3 Group Velocity for All Frequencies

Overall, three calculations were done to find the average group velocity of the spin wave pulse traveling down the length of the sample for different driving frequencies. The values are listed in table 4.2 and compared in Fig. 4.18. The predicted group velocities found using the cross-correlation method for both the single pulse and the average pulse are within the same uncertainty. The predicted group velocities found using the dispersion relation are outside the uncertainties of the predicted group velocities using the cross-correlation method. The percent difference between the predicted group velocity using the single pulse and average pulse from cross-correlation and the dispersion relation is 19% and 20% respectively. A potential reason for the discrepancy is the simple model used does not include all the potential complex dynamics of the spin wave pulse traveling. For example, the reflections off the grooves are not taken into consideration. Also, the contribution of the higher mode group velocities is not accounted for.

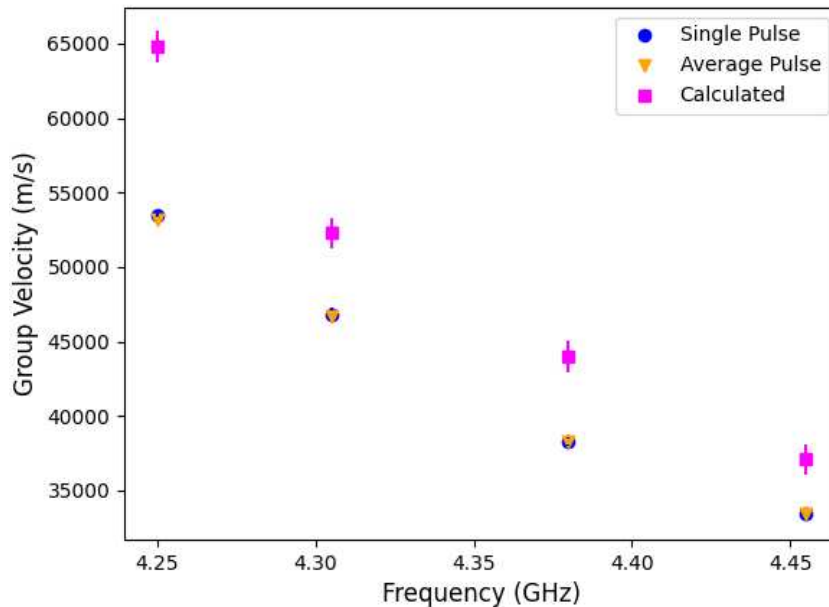


Figure 4.18: The average group velocity at each frequency. The cross-correlation method is used to calculate the group velocity using the single pulse and the average pulse as the reference pulse. The dispersion relation in Fig. 4.16 is used to obtain the calculated group velocities at each frequency. The group velocities obtained using the single pulse are blue, the orange points used the average pulse, and the group velocities calculated from the dispersion relation are the pink points.

Table 4.2: Table of the group velocities obtained using the single pulse and average pulse cross-correlation time lags, and calculated using the dispersion relation for all frequencies.

Single Pulse	
Frequency	Group Velocity (m/s)
BP	53500 ± 200
BG1	46800 ± 500
BG2	38300 ± 300
BG3	33400 ± 80
Average Pulse	
Frequency	Group Velocity (m/s)
BP	53200 ± 200
BG1	46700 ± 400
BG2	37700 ± 200
BG3	33300 ± 100
Calculated	
Frequency	Group Velocity (m/s)
BP	64800 ± 1000
BG1	52200 ± 1000
BG2	44000 ± 1000
BG3	37100 ± 1000

4.6 Pulse Shape

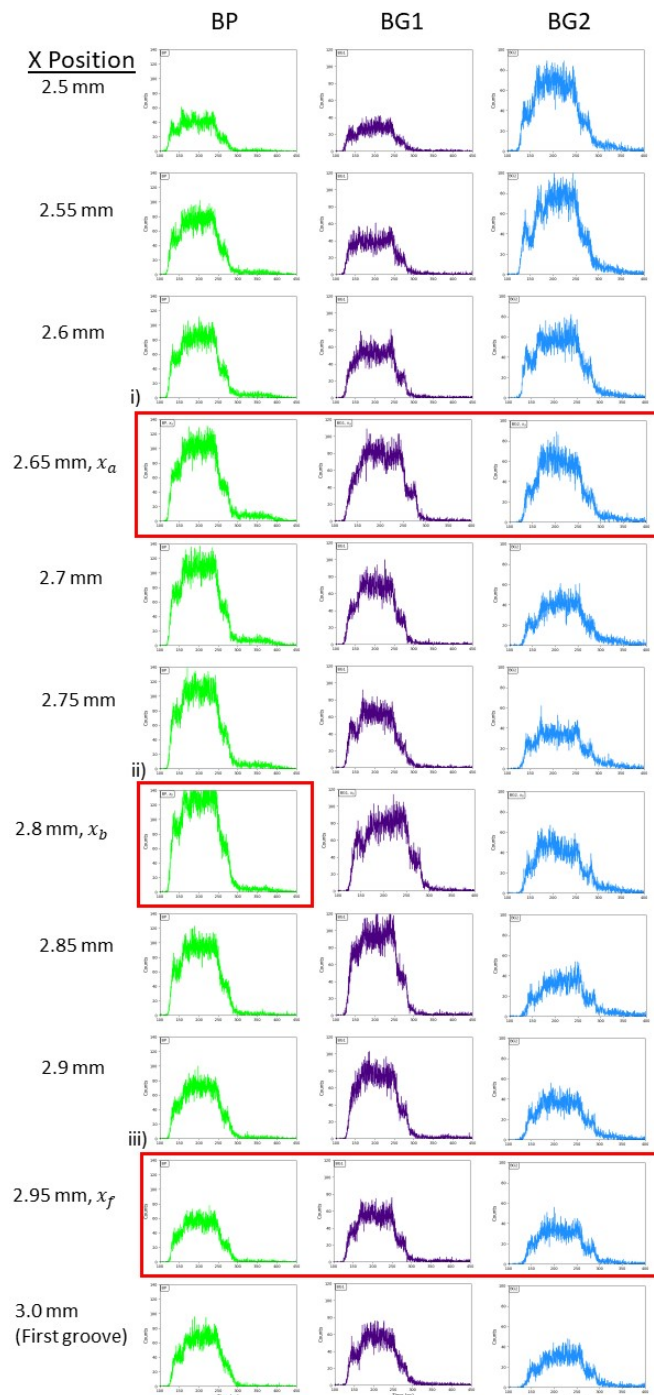


Figure 4.19: Plots showing the raw pulse data for different x positions, at $y = y_2$, before the first groove. The green pulses are from the BP. The purple pulses are from the BG1, and the blue pulses are from BG2. The red boxes (i,ii,iii) highlight the specific pulses used in the pulse shape analysis. i) is used to analyze the effect the different spin wave modes group velocities on the pulse shape. ii) is the single pulse used in the cross-correlation method in section 4.5.1. iii) is the pulses right before the first groove at $x = 3.0$ mm.

Next, the evolution of the pulse shape will be discussed. Fig. 4.19 shows all the pulses obtained at locations leading up to the first groove at $x = 3.0$ mm, down the center width of the sample where $y = y_2$. The green pulses are from the BP, purple pulses from BG1, and blue pulses from BG2. The labeled red boxes (i, ii, iii) highlight specific positions of interest that will be discussed. The BG3 pulse at position x_a in Fig. 4.20 has a maximum count of 20. While the pulses in Fig. 4.19 at position x_a have maximum counts ranging from 110-140. So, the pulses from BG3 are omitted in this portion of the analysis due to the difficulty in identifying pulse features. First the FWHM from the cross-correlation amplitudes will be examined to look at the pulse spreading. Then features of the pulse shape, like tails at the end of the pulse and jumps in the pulse counts, will be discussed.

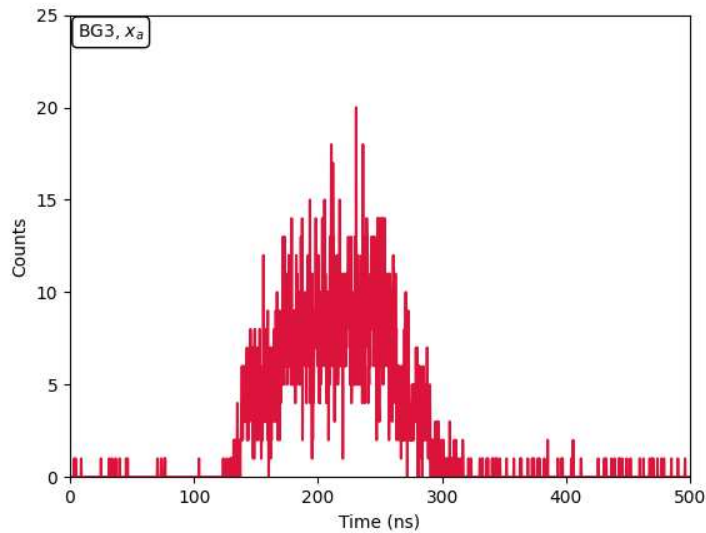


Figure 4.20: Raw data for BG3 at $x = x_a$ and $y = y_2$.

4.6.1 Pulse Spreading

The FWHM from the cross-correlation is obtained to determine if there is significant pulse spreading down the length or not. Pulse spreading could occur for the band pass dataset, in particular, if there are sizeable lingering reflections from the patterning. Fig. 4.21 shows the FWHM values extracted from the cross-correlation results for each position along the length for all fre-

quencies. The red dashed line is the FWHM from the autocorrelation. The FWHM values vary more along the length for the driving frequencies BP, BG1, BG2, and BG3 (Fig. 4.21) as compared to the minimal variation found across the width (Fig. 4.9). The FWHM down the length, for all frequencies, shows dramatic increases in several locations for $x > 6.5$ mm. This could be due to the reflections off the end of the sample that cause the pulse shape and counts to change.

The orange points are associated with regions where the counts are low, and the blue points are associated with regions with higher counts and the FWHM values range from 145 ns to 155 ns. At the BG3 frequency there is minimal change in the FWHM, but these measurements are less reliable because the counts are lower than at other frequencies, so the cross-correlation is more difficult. The FWHM of the cross-correlation does not deviate significantly from the FWHM of the autocorrelation, so the pulse shape is mostly consistent as it travels down the sample. A potential reason why the pulse shape does not change is because the reflections are weak and with the multimode response the cross-correlation does not pick up on these changes near the beginning of the crystal ($x < 6.4$ mm).

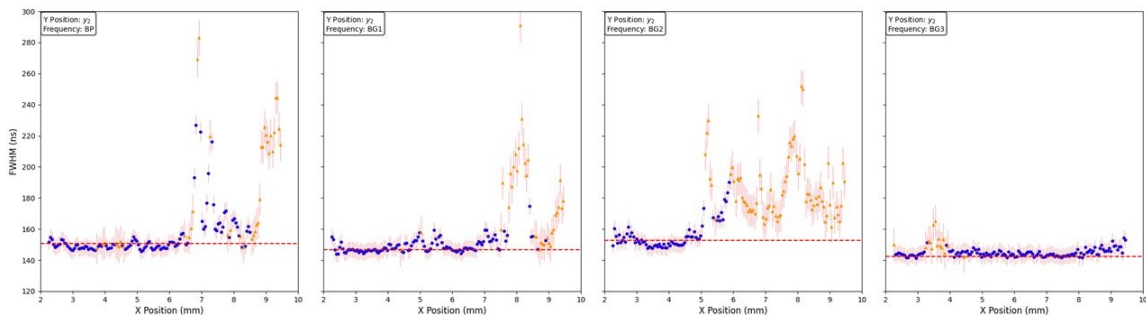


Figure 4.21: A comparison of the FWHM of the cross-correlation amplitude down the length of the sample for every frequency. The blue points are data points with higher counts and the orange points are data points with lower counts. The red dashed line is the average FWHM of the blue points.

4.6.2 Pulse Shape Changes

This section focuses on analyzing the TR-BLS data to look for more subtle changes to the pulse shape changing. Figs. 4.22 a), b), and c) show the pulse intensity traveling down the center

of the crystal (y_2) for the BP, BG1, and BG2. The intensity scales have been adjusted to account for the efficiency of the antenna, which is diminished with increasing wavevector and hence also with increasing frequency. At each position, the pulse was shifted by the group velocity to choose specific times to focus on the pulse shape more carefully. Specifically, the pulses at $x = x_a$ (red box i), for different times, will be analyzed to show the effects of the spin wave modes' different group velocities have on the pulse shape. Shifting the pulse by the group velocity helps to identify changes in the pulse shape and, as will be shown, to identify changes in the pulse propagation pattern. The reflected pulse, which is the pulse that has reflected from the end of the sample, is identified in Fig. 4.22 and in subsequent figures.

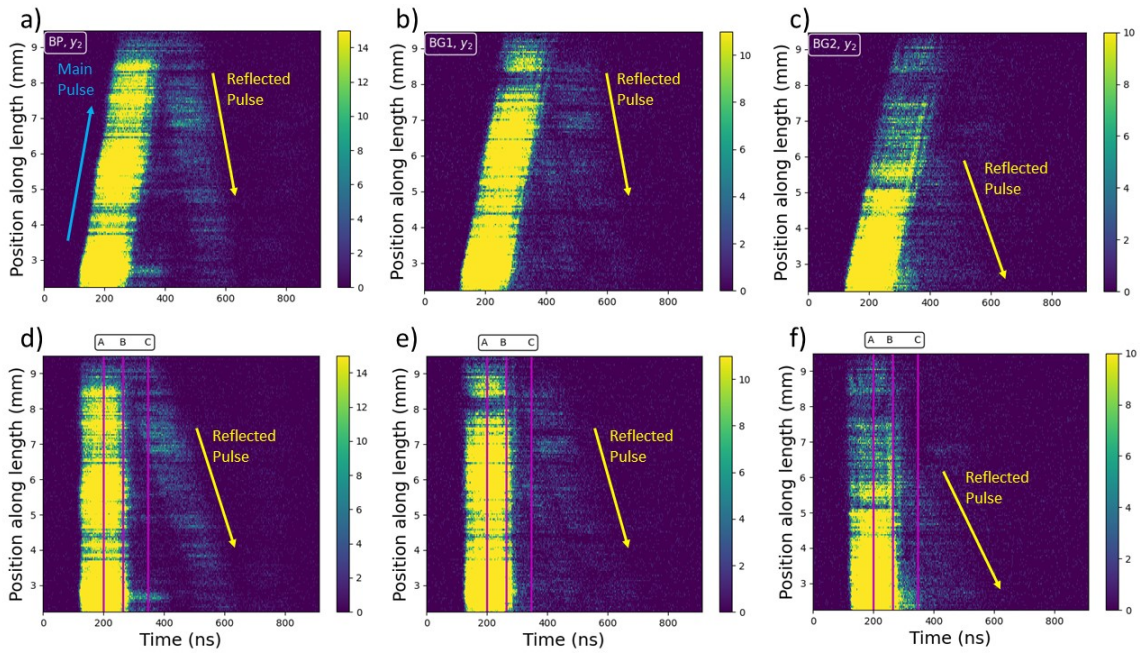


Figure 4.22: The top row are the plots tracking the position of the spin wave pulse over time. The intensity scale has been adjusted to account for the antenna excitation efficiency. The bottom row are the same graphs tracking the position of the spin wave pulse over time, but shifted by the average group velocity. Three times are identified to further explore the pulse shape changing (time A = 200 ns, time B = 265 ns, time C = 347.5 ns).

After shifting the pulse by the average group velocity, images of the pulse propagation pattern were constructed at selected times marked as A, B, and C in Fig. 4.22. The pulse at a fourth time (80 ns, before the arrival of the pulse) was also used to verify no counts were present. Time A

(200 ns), was selected because it is near the mid-point of the pulse. At time B (265 ns) the main pulse starts to leave. Lastly, at time C (347.5 ns) the main pulse has left, but the reflected pulse has not returned to the front of the crystal yet. In Fig. 4.22 d) and f), there is some energy left before the first groove ($x = 3.0$ mm) at time C. This could be caused by modes that have later arrival times, or by constructive interference from the reflections off the grooves, or both. To better understand the cause of the trapped energy before the first groove, the plots of the pulse shape spatially and temporally were constructed at specific times. Fig. 4.23 compares the pulses spatially for time A, B, and C.

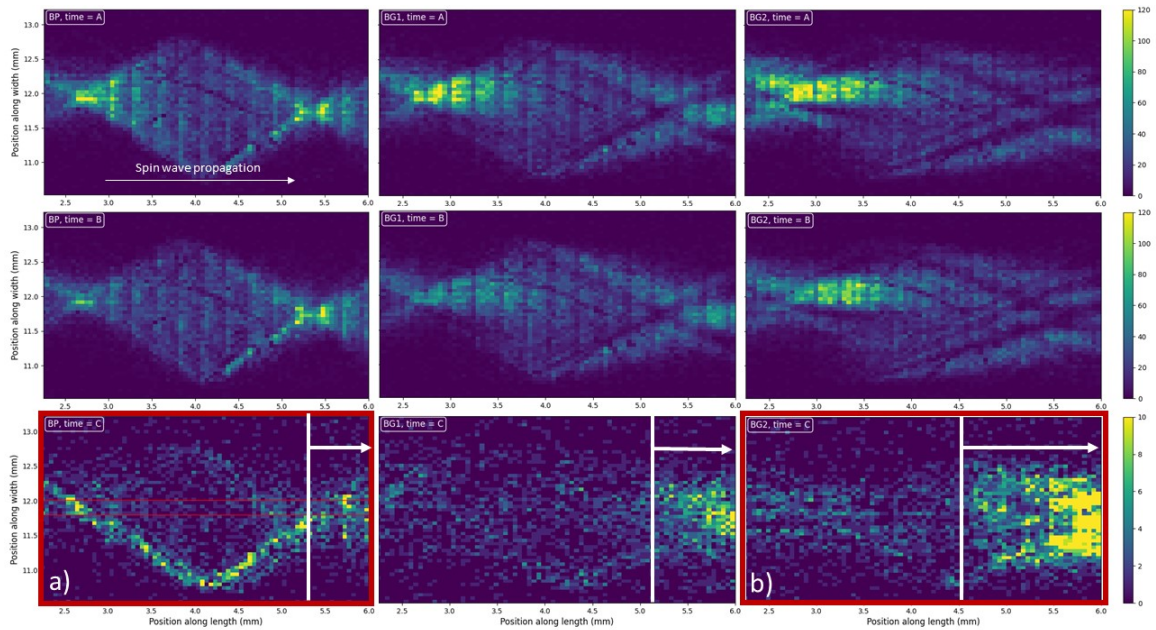


Figure 4.23: Spin wave propagation patterns for each frequency (BP, BG1, BG2 from left to right) at times A, B, and C. The intensity scales for time C have been adjusted by a factor of 12 to better highlight features. The range has been adjusted, from $x = 2.25$ mm to 6.0 mm, and is an abbreviated version of data as compared to Fig. 4.22 where the range is from $x = 2.25$ mm to 9.5 mm, chosen to better show features at the beginning of the crystal. On the bottom row, counts to the right of the arrow are from the reflected pulse and should be disregarded.

The main pulse starts around 125 ns and has a pulse duration of 200 ns and is expected to end around 325 ns. However, at time C, for the BP (Fig. 4.23 a) there is an outline of the diamond pattern that lingers beyond the duration of the excitation applied at the antenna. This diamond

outline looks like the modeled example in Fig. 4.12. This change in the diamond pattern from a filled diamond at time A to an outlined diamond at time C is, at least in part, due to a change in the width-quantized modes that are present. At the BP frequency, the higher mode wavevectors have slower group velocities as compared to the lower width-quantized modes (see Fig. 4.17 for the group velocity from the dispersion relation) and arrive later and are still present after the main mode group velocity ($n = 1$) has passed.

The dispersion relations for the YIG microstrip can be used to understand the frequencies of the band gaps in the 1D magnonic crystal, and to determine the cause of the change in the observed spin wave propagation pattern from time A to C.

$$k_{a,b,c,d} = \frac{n\pi}{d} \quad (4.6)$$

First, to understand the reason for the formation of the observed band gaps, the wavevectors ($k_{a,b,c,d}$) that correspond to destructive interference when reflected off the grooves are calculated (equation 4.6). Where d is the distance between the grooves and the condition for destructive interference of the reflected waves with the incident wave. These key wavevectors are shown in Fig. 4.24 superimposed on the width-quantized surface wave dispersion relations, where $d = 275 \mu\text{m}$, the repetition rate for the grooves, was used to calculate $k_{a,b,c,d}$. The uncertainty can be estimated by considering the groove widths as the uncertainty in $d \pm 25 \mu\text{m}$. The d value ranges are shown in Fig. 4.1

The wavevectors $k_{a,b,c,d}$ that are associated with destructive interference are plotted on the dispersion relation (the highlighted regions in Fig. 4.24). The specific modes that fall within each of these wavevector ranges at a particular frequency can be found by looking for the intersection of the $k_{a,b,c,d}$ shaded regions and the dashed lines for the frequencies on Fig. 4.24. For example, as shown in table 4.3 at the BP frequency, the modes that overlap with wavevector k_a are modes 9 and 11. The width-quantized wavevectors for the corresponding modes using equation 4.3 are also included table 4.3. This process is repeated to calculate $k_{a,b,c,d}$ for the BP, BG1, and BG2. The results are summarized in tables 4.3, 4.4, and 4.5.

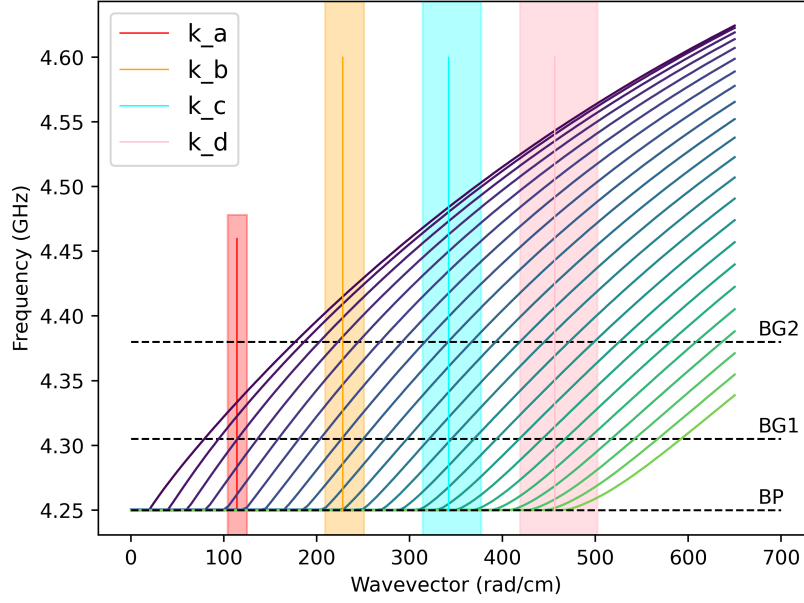


Figure 4.24: The width-quantized surface wave dispersion relations for the YIG film with the wavevectors that corresponds to destructive interference $k_{a,b,c,d}$ (lines). The shaded regions show the uncertainties. The black dashed lines show the intersection of BP, BG1, and BG2 with the wavevectors.

Table 4.3: Table of the calculated $k_{a,b,c,d}$ values, and the mode numbers that intersect each wavevector the BP. k_n is the calculated width-quantized wavevector. The highlighted sections are the potential higher order modes and their corresponding width wavevector contributing to the open diamond pattern in Fig. 4.25

BP	$k_{a,b,c,d}$ Range (rad/cm)	modes (n)	k_n calculated (rad/cm)
k_a	104, 114, 125	9, 11	70, 84
k_b	209, 228, 251	19, 21, 23	140, 154, 168
k_c	314, 343, 377	29, 31, 33, 35	209, 229, 237, 251
k_d	419, 457, 502	41, 43, 45	293, 307, 321

Table 4.4: Table of the calculated $k_{a,b,c,d}$ values, and the mode numbers that intersect each wavevector the BG1. k_n is the calculated width-quantized wavevector.

BG1	$k_{a,b,c,d}$ Range (rad/cm)	modes (n)	k_n calculated (rad/cm)
k_a	104, 114, 125	5	42
k_b	209, 228, 251	15, 17	112, 126
k_c	314, 343, 377	23, 25, 27	168, 182, 195
k_d	419, 457, 502	31, 33, 35, 37	223, 237, 251, 265

Table 4.5: Table of the calculated $k_{a,b,c,d}$ values, and the mode numbers that intersect each wavevector the BG2. k_n is the calculated width-quantized wavevector.

BG2	$k_{a,b,c,d}$ Range (rad/cm)	modes (n)	k_n calculated (rad/cm)
k_a	104, 114, 125	n/a	n/a
k_b	209, 228, 251	7, 9	56, 70
k_c	314, 343, 377	15, 17, 19	112, 126, 140
k_d	419, 457, 502	23, 25, 27, 29	168, 182, 195, 209

For BP1, k_a overlaps with mode $n = 5$ and for BP2, k_a overlaps with the low modes $n = 7$ and 9. Since lower modes are the dominant modes for pulse propagation, the destructive interference from these modes leads to the observed band gaps in the transmission profile from the microwave measurements (Fig. 3.2).

The dispersion relation also provides more insight to the evolution of the diamond pattern at the BP frequency in Fig. 4.23 To understand this, the dominant wavevector in Fig. 4.23 a) is estimated by determining the size along y of the dominant feature, as illustrated in Fig. 4.25. The length α can be converted to a dominant wavevector using:

$$k_\alpha = \frac{\pi}{\alpha} = 149 \frac{rad}{cm} \quad (4.7)$$

The width wavevector (k_α) from the diamond pattern is compared to the calculated k_n values to determine what modes contribute to creating the diamond outline. The wavevector (k_α) for the width of the diamond pattern is 149 rad/cm. For the BP, k_α falls between wavevectors 140 and 154 (mode $n = 19$ and 21) Therefore, the dominant modes that exist at time C and cause the diamond outline are modes 19 and 21 and higher.

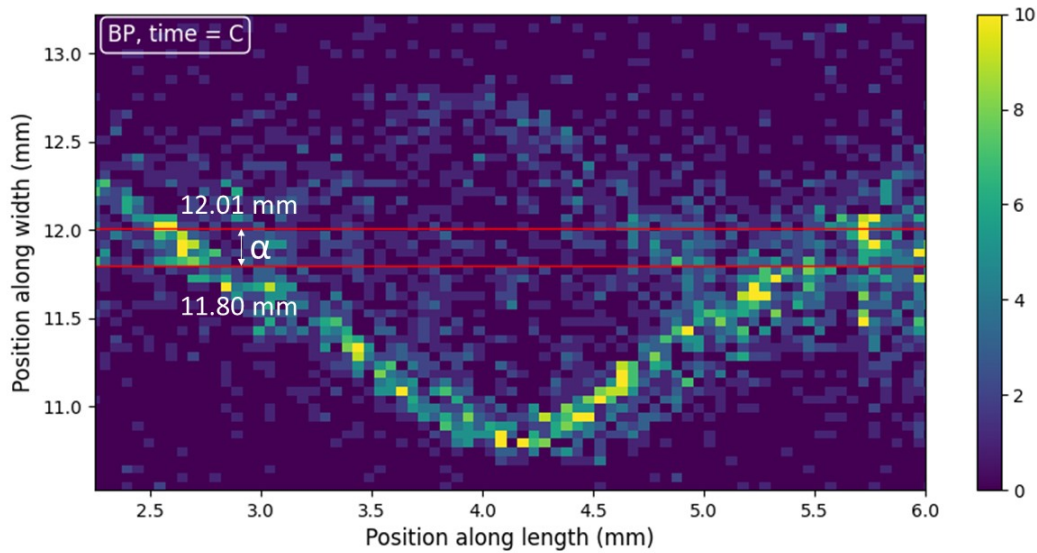


Figure 4.25: The figure highlighted in the red box from Fig. 4.23. The width of the diamond pattern is indicated by α . ($k_\alpha = 149$ rad/cm.)

Based on Fig. 4.25, it appears that the modes with $n < 19$ have passed but some modes with $n > 19$ remain at time C. To determine whether this is an effect that stems from the mode group velocities or from reflections, the group velocities for each mode were used to predict the potential contribution of each of the modes to pulse shape, and hence to determine which modes should exist as direct arrivals at time C. Fig. 4.26 a), b), and c) show the predicted pulse arrival time ranges for each mode, calculated using their group velocity, at position x_a . The pulse duration is 200 ns. The first mode arrival time is set to 125 ns to match the TR-BLS data. The amplitude for each pulse is $1/n$, where n is the mode number. As shown in Fig. 4.26 a), the higher modes for the BP

create a tail at the end of the pulse. This tail is also seen in the raw pulse data (Fig. 4.26 d) and lies within the same time range as the higher modes plotted based on arrival time, which is highlighted by the red dashed lines. This matches the assertion that the counts detected at later times are due to the higher modes that arrive and pass by later than the dominant $n = 1$ mode. This is a simple model and does not include any other factors that may affect the pulse amplitude, like reflections and constructive and destructive interference.

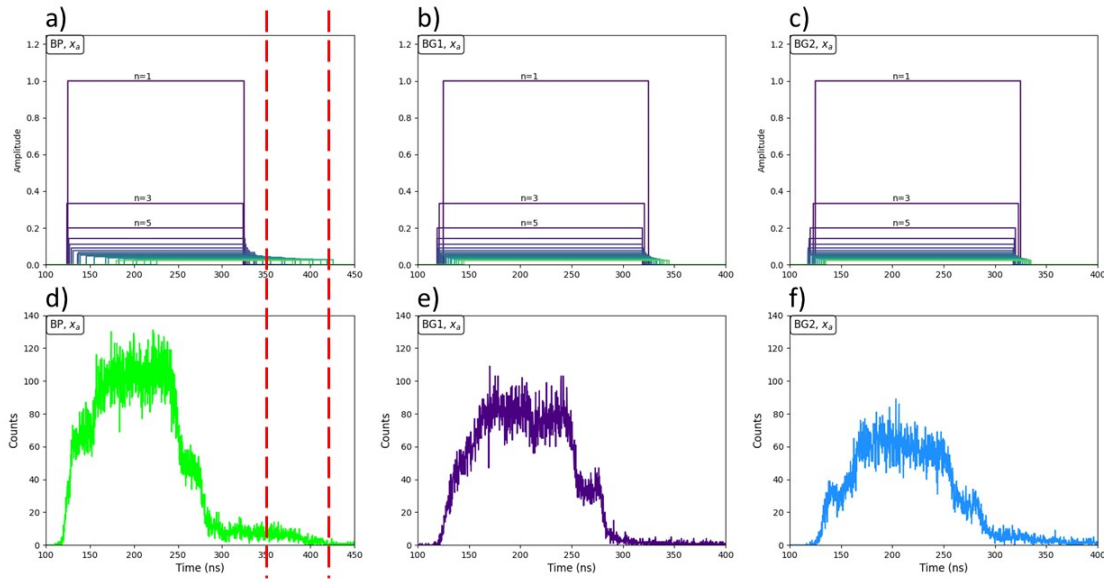


Figure 4.26: Fig. a), b), and c) are the pulses for each mode plotted based on arrival time at position x_a . Fig. d), e), and f) are the raw pulses for the BP (green pulse), BG1 (purple pulse), and BG2 (blue pulse). The red dashed lines show the time range for the higher modes plotted based on arrival time and raw pulse for the BP lie within the same time range.

The modes that can exist after time C for the BP frequency are plotted more explicitly in Fig. 4.27 a). The purple dashed line is where the $n = 1$ group velocity would be for reference. The red dashed line is to show time C for the modes. Fig. 4.27 b) is a zoomed in version of Fig. 4.27 a). As seen in Fig. 4.27 b) the lowest mode that can exist at time C is mode $n = 21$. This matches the expected modes ($n = 19$ and $n = 21$) from the k_α calculation. The higher modes create a tail at the

end of the pulse for the calculations and raw TR-BLS data in Figs. 4.26 a) and d) and can also be seen in Fig. 4.22 d) as a bright horizontal line before the first groove ($x = 3.0$ mm).

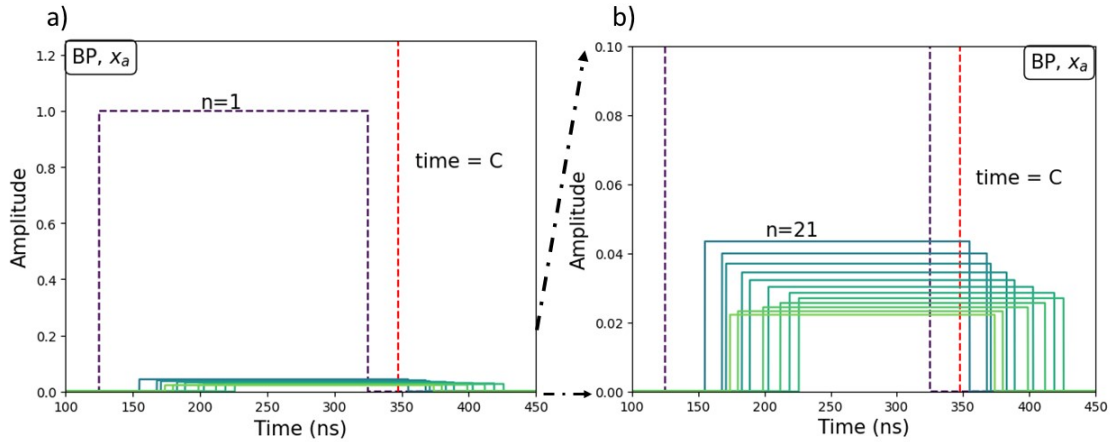


Figure 4.27: The higher mode group velocities at the BP frequency that can exist at time = C. The purple dotted line shows the time range for the $n=1$ mode. The red dotted line shows the location of time = C. b) is the zoomed in version of Fig. a) and The dashed black line indicates a change in scale between a) and b).

At first glance, the pulse features for the BP and BG2 frequencies look very similar. In Fig. 4.22 f) for the BG2 frequency, there are counts lingering before the first groove ($x = 3.0$ mm) and the pulse in Fig. 4.22 f) has a tail, both of which are features seen with the BP. However, when looking at Fig. 4.23 b) the lingering counts do not form a diamond outline. Also, in Fig. 4.26 c), the higher modes do not arrive as long after the main pulse as they do for the BP. Therefore, the counts detected at time C for BG1 and BG2 are not caused by higher modes that arrive and depart later, and are more likely caused by residual multiple reflections from the grooves that are at least in part constructive.

4.7 Potential Future Analysis

Future analysis of the 1D magnonic crystal includes working towards a better understanding of the causes for the pulse shapes. For example, Fig. 4.28 shows the pulses right before the grooves for the BP, BG1, and BG2, but when the pulse shapes in Fig. 4.28 are compared to pulses in Fig. 4.19 at position x_b , one can see that the pulses in Fig. 4.28 do not have the same shelf feature on the falling edge of the pulse. This pulse shelf deformation happens consistently for pulses right before the groove at x positions x_f , x_g , and x_h . The reason for these differences in the pulse shapes is not fully understood. A potential method to further analyze the data would be to update the simple model used for calculating the group velocity modes to include reflections.

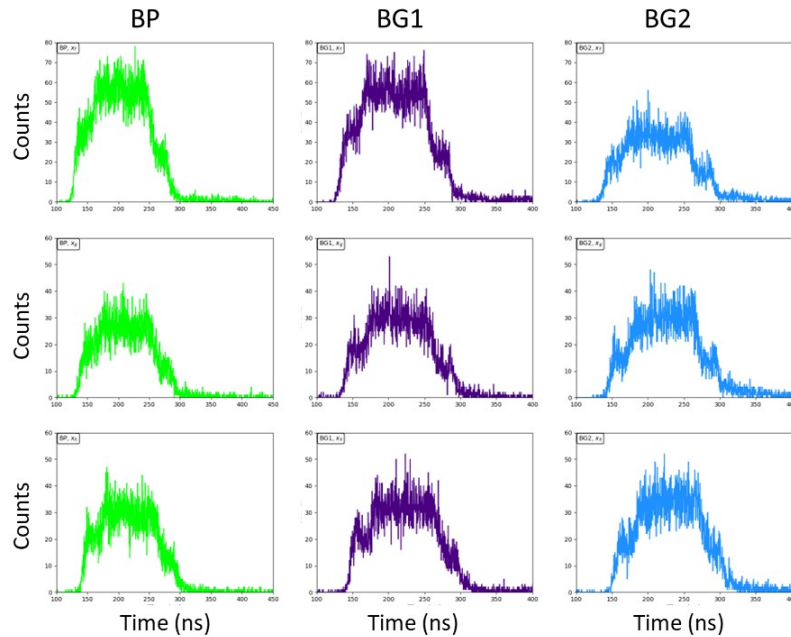


Figure 4.28: A comparison of all the pulses at the positions near the grooves at x positions x_f , x_g , and x_h . The pulses measured at the BP, BG1, and BG2 are shown in green, purple, and blue, respectively.

Chapter 5

Conclusion

In summary, time-resolved-BLS (TR-BLS) measurements were used to investigate spin wave propagation in a one-dimensional magnonic crystal for a magnetostatic surface wave configuration where the magnetization is in-plane and perpendicular to the direction of the spin wave propagation. A cross-correlation analysis technique was used to obtain the average group velocity and to assess changes in the spin wave pulse shape. Microwave and TR-BLS measurements confirm that the structure of the 1D magnonic crystal leads to the formation of band gaps in the transmission profile where the spin wave transmission is suppressed, which is expected for a 1D magnonic crystal. The TR-BLS measurements show differences in the pulse propagation characteristics for frequencies at the band pass and band gaps. The measured average group velocities obtained from the cross-correlation showed a trend of decreasing velocity with increasing frequency that is consistent with values calculated from the dispersion relation. However, the measured values were consistently approximately 20% lower than the predicted values.

Two dimensional scans of the spin wave propagation patterns were obtained using the TR-BLS, and one of the most striking features of the spin wave images is the propagation pattern, which show two-dimensional patterns that look nothing like what one would be expected for a plane wave in a structure with one-dimensional patterns. This is important because models developed to describe the performance of a 1D magnonic crystal typically start by assuming that the spin waves, like the crystal, are also purely one-dimensional. The TR-BLS measurements show a diamond-shaped pattern, which forms because multiple width-quantized spin wave modes are excited simultaneously by the stripline antenna. The presence of multiple modes leads to more complex behavior not just spatially but also in the time domain. At the BP frequency, lingering higher modes are observed, as evidenced by the evolution of the spin wave pattern from a filled diamond during the pulse to an outline of a diamond on the back end of the pulse and a visible tail on the pulse in the time domain. This is due to the later arrival time of higher-order width-

quantized modes that have slower group velocities. The pulse shape at BG2 also has a trailing tail. However, there is no diamond pattern outline in the spatial graphs. Therefore, the trailing tail for the BG2 pulses are most likely the result of interference of the multiple reflected pulses that is at least partially constructive.

TR-BLS measurements are rich with information on spin wave propagation. The model used to examine the roles of the different modes in this thesis was simplified. Future work to update the model to include more complex dynamics like constructive and destructive wave interference behavior from reflections is needed in order to better understand the roles the different modes have on the overall pulse shape and average group velocity of spin waves in 1D magnonic crystals.

Acknowledgement: The sample was provided by Cesar Ordonez (UNAM), some of the data collected by group member Mitchell Swyt, and I also acknowledge helpful conversations with Jason Liu (Georgia Southern University). This work was supported by NSF EFMA-1741666.

Bibliography

- [1] A. Mahmoud, F. Ciubotaru, F. Vanderveken, A. V. Chumak, S. Hamdioui, C. Adelman, and S. Cotofana, “Introduction to spin wave computing,” *Journal of Applied Physics*, vol. 128, no. 16, p. 161101, 2020.
- [2] A. V. Chumak, A. A. Serga, and B. Hillebrands, “Magnonic crystals for data processing,” *Journal of Physics D: Applied Physics*, vol. 50, p. 244001, May 2017.
- [3] A. A. Serga, A. V. Chumak, and B. Hillebrands, “YIG magnonics,” *Journal of Physics D: Applied Physics*, vol. 43, p. 264002, Jun 2010.
- [4] T. Sebastian, K. Schultheiss, B. Obry, B. Hillebrands, and H. Schultheiss, “Micro-focused Brillouin light scattering: imaging spin waves at the nanoscale,” *Frontiers in Physics*, vol. 3, p. 35, 2015.
- [5] O. Büttner, M. Bauer, S. O. Demokritov, B. Hillebrands, Y. S. Kivshar, V. Grimalsky, Y. Rapoport, and A. N. Slavin, “Linear and nonlinear diffraction of dipolar spin waves in yttrium iron garnet films observed by space- and time-resolved Brillouin light scattering,” *Phys. Rev. B*, vol. 61, pp. 11576–11587, May 2000.
- [6] Y. Zhu, ed., *Brillouin light scattering spectroscopy*, pp. 543–578. Boston, MA: Springer US, 2005.
- [7] M. B. Jungfleisch, W. Zhang, W. Jiang, H. Chang, J. Sklenar, S. M. Wu, J. E. Pearson, A. Bhattacharya, J. B. Ketterson, M. Wu, and A. Hoffmann, “Spin waves in micro-structured yttrium iron garnet nanometer-thick films,” *Journal of Applied Physics*, vol. 117, p. 17D128, Mar 2015.
- [8] J. Trossman, J. Lim, W. Bang, J. B. Ketterson, and C. C. Tsai, “Phase detection of spin waves in yttrium iron garnet and metal induced nonreciprocity,” *Journal of Applied Physics*, vol. 125, p. 053905, Feb 2019.

- [9] V. V. Kruglyak, S. O. Demokritov, and D. Grundler, “Magnonics,” *Journal of Physics D: Applied Physics*, vol. 43, p. 264001, Jun 2010.
- [10] E. Hecht, *Optics*. Harlow, England: Pearson Education, 5th ed., 2017.
- [11] J. R. Eshbach and R. W. Damon, “Surface magnetostatic modes and surface spin waves,” *Phys. Rev.*, vol. 118, pp. 1208–1210, Jun 1960.
- [12] D. D. Stancil and A. Prabhakar, *Introduction to Magnetism*, pp. 1–31. Boston, MA: Springer US, 2009.
- [13] B. Obry, P. Pirro, T. Brächer, A. V. Chumak, J. Osten, F. Ciubotaru, A. A. Serga, J. Fassbender, and B. Hillebrands, “A micro-structured ion-implanted magnonic crystal,” *Applied Physics Letters*, vol. 102, p. 202403, May 2013.
- [14] H. Qin, S. J. Hämäläinen, K. Arjas, J. Witteveen, and S. van Dijken, “Propagating spin waves in nanometer-thick yttrium iron garnet films: Dependence on wave vector, magnetic field strength, and angle,” *Phys. Rev. B*, vol. 98, p. 224422, Dec 2018.
- [15] W. Song, X. Wang, W. Wang, C. Jiang, X. Wang, and G. Chai, “Backward magnetostatic surface spin waves in coupled Co/FeNi bilayers,” *Physica Status Solidi (RRL) – Rapid Research Letters*, vol. 14, no. 8, p. 2000118, 2020.
- [16] C. Kittel, *Introduction to solid state physics*. Hoboken, NJ: Wiley, 8th ed., 2005.
- [17] S. Nikitov, P. Tailhades, and C. Tsai, “Spin waves in periodic magnetic structures—magnonic crystals,” *Journal of Magnetism and Magnetic Materials*, vol. 236, no. 3, pp. 320–330, 2001.
- [18] M. Butt, S. Khonina, and N. Kazanskiy, “Recent advances in photonic crystal optical devices: A review,” *Optics Laser Technology*, vol. 142, p. 107265, 2021.
- [19] *Magnonics from fundamentals to applications*. Topics in Applied Physics, v. 125., Berlin ;: Springer, 2013.

- [20] H. Zhang, S. Krooswyk, and J. Ou, “Chapter 5 - measurement and data acquisition techniques,” in *High Speed Digital Design* (H. Zhang, S. Krooswyk, and J. Ou, eds.), pp. 199–219, Boston: Morgan Kaufmann, 2015.
- [21] J. G. Dil, “Brillouin scattering in condensed matter,” *Reports on Progress in Physics*, vol. 45, p. 285, Mar 1982.
- [22] O. Büttner, M. Bauer, A. Rueff, S. Demokritov, B. Hillebrands, A. Slavin, M. Kostylev, and B. Kalinikos, “Space- and time-resolved Brillouin light scattering from nonlinear spin-wave packets,” *Ultrasonics*, vol. 38, no. 1, pp. 443–449, 2000.
- [23] J. R. Sandercock, *Tandem Fabry-Perot Spectrometers TFP-1 and TFP-2 HC, Operator Manual*. JRS Optical Instruments.
- [24] I. R. Kenyon, *The light fantastic: a modern introduction to classical and quantum optics*. Oxford :: Oxford University Press, 2nd ed., 2011.
- [25] R. N. Bracewell, *The Fourier transform and its applications*. McGraw-Hill electrical and electronic engineering series., New York: McGraw-Hill, 2d ed. ed., 1978.
- [26] G. Zebende, “DCCA cross-correlation coefficient: Quantifying level of cross-correlation,” *Physica A: Statistical Mechanics and its Applications*, vol. 390, no. 4, pp. 614–618, 2011.
- [27] V. E. Demidov, S. O. Demokritov, K. Rott, P. Krzysteczko, and G. Reiss, “Mode interference and periodic self-focusing of spin waves in permalloy microstripes,” *Phys. Rev. B*, vol. 77, p. 064406, Feb 2008.
- [28] Z. Zhang, M. Vogel, J. Holanda, J. Ding, M. B. Jungfleisch, Y. Li, J. E. Pearson, R. Divan, W. Zhang, A. Hoffmann, Y. Nie, and V. Novosad, “Controlled interconversion of quantized spin wave modes via local magnetic fields,” *Phys. Rev. B*, vol. 100, p. 014429, Jul 2019.

- [29] B. A. Kalinikos and A. N. Slavin, "Theory of dipole-exchange spin wave spectrum for ferromagnetic films with mixed exchange boundary conditions," *Journal of Physics C: Solid State Physics*, vol. 19, p. 7013, Dec 1986.